ORNL/TM-9533

ornl

OAK RIDGE NATIONAL LABORATORY

MARTIN MARIETTA

Plasma Engineering Analysis of a Small Torsatron Reactor

J. T. Lacatski
W. A. Houlberg
N. A. Uckan

OPERATED BY
MARTIN MARIETTA ENERGY SYSTEMS, INC.
FOR THE UNITED STATES
DEPARTMENT OF ENERGY

ORNL/TM-9533
Dist. Category UC-20

ORNL/TM--9533

DE86 001469

Fusion Energy Division

PLASMA ENGINEERING ANALYSIS OF A SMALL TORSATRON REACTOR

J. T. Lacatski
W. T. Houlberg
N. A. Uckan

Date Published - October 1985

Prepared by the
OAK RIDGE NATIONAL LABORATORY
Oak Ridge, Tennessee 37831
operated by
MARTIN MARIETTA ENERGY SYSTEMS, INC.
for the
U.S. DEPARTMENT OF ENERGY
under Contract No. DE-AC05-84OR21400

TABLE OF CONTENTS

LIST OF TABLES

LIST OF FIGURES

FIGURE PAGE

FIGURE PAGE

ABSTRACT

This study examines the plasma physics and reactor engineering feasibility of a small, medium aspect ratio, high-beta, $\ell=2$, D-T torsatron power reactor, based on the magnetic configuration of the Advanced Toroidal Facility, Oak Ridge National Laboratory. Plasma analyses are performed to assess whether confinement in a small, average radius plasma is sufficient to yield an ignited or high-Q driven device. Much of the physics assessment focuses on an evaluation of the radial electric field created by the nonambipolar particle flux. Detailed transport simulations are done with both fixed and self-consistent evolution of the radial electric field. Basic reactor engineering considerations taken into account are neutron wall loading, maximum magnetic field at the helical coils, coil shield thickness, and tritium breeding blanket-shield thickness.

In stellarator/torsatron transport modeling, the transition from an intermediate collisionality regime in which confinement decreases with increasing temperature (decreasing collisionality) to the low collisionality regime in which confinement improves with lower collisionality is shown to be of particular importance. Using a model that joins these two collisionality regimes to the resonant transition regime, where the $\vec{E} \times \vec{B}$ and $\vec{B} \times \nabla B$ drifts cancel, electron losses are found to be the dominant factor in determining the radial electric field once the low collisionality regime is entered. Since ion confinement is greatly improved once electron losses dominate, investigations are made into the impact of the magnitude of the radial electric field, the varying effects of ion cyclotron and electron cyclotron heating methods, and the influence of additional anomalous electron losses during startup.

These analyses lead to a small, steady-state torsatron reactor of 100 cm average plasma radius, aspect ratio 7, 9% beta, 5 tesla axial magnetic field, with 2.3 MW/m^2 wall loading. At an assumed net efficiency of 33%, ~306 MWe is produced. Plasma performance in this small reactor is found to be very dependent on the presence of a moderate-to-strong radial electric field. Nominal values of all basic reactor engineering parameters are found which satisfy feasibility constraints, with the possible exception of completely adequate shielding directly under the helical coils.

CHAPTER I

INTRODUCTION

Stellarator/torsatron reactors have the qualitative advantages of zero net plasma current, steady-state magnetic fields and thermonuclear burn, and potential for ignited operation. The steady-state magnetic flux surfaces and rotational transform profile are determined by currents in external windings rather than inside the plasma as in tokamaks. Initial ionization and plasma startup therefore occurs on existing vacuum magnetic surfaces. Steady-state operation eliminates thermal cycling of reactor components, and zero net plasma current eliminates the possibility of intense magnetic energy deposition on the first wall due to a disruption. Plasma operation at high Q or at ignition may be possible.

In Table I, plasma and machine parameters of five previous stellarator/torsatron power reactor studies are listed: the Massachusetts Institute of Technology T-2 torsatron, the Mitsubishi Industries (Japan) Heliotron-H, the Kharkov Physico-Technical Institute (USSR) TNPP torsatron, the University of Wisconsin UWTOR-M torsatron, and the Los Alamos National Laboratory MSR-IIB stellarator.

As shown in Table I, past stellarator/torsatron power reactor designs have tended toward large aspect ratios (>12) with major radii in excess of 20 m.[1,2] The economic attractiveness of power reactors of this size is questionable.[3] The purpose of this study is to examine the feasibility of a small, medium aspect ratio, high-beta, $\ell = 2$, deuterium-tritium (D-T) torsatron power reactor based upon the magnetic configuration properties of the Advanced Toroidal Facility

Table I. Stellarator/Torsatron Power Reactor Designs

	MIT T-2	Japan Heliotron-H	USSR TNPP	UW UWTOR-M	LANL MSR-IIB
Plasma radius (m)	1.5	1.7	2.1	1.72	0.81
Major radius (m)	24.0	21.0	36.8	24.1	23.0
Aspect ratio	16	12.4	17.5	14.0	28.4
Plasma volume (m^3)	1067	1198	3203	1407	298
Average density ($10^{20}/m^3$)	2.5	1.17	2.5	1.46	3.64
Average beta	0.065	0.06	0.1	0.06	0.08
On-axis magnetic field (T)	5.0	4.0	4.4	4.5	6.56
Peak field at coil (T)	9	9	—	11.6	11.6
First-wall loading (MW/m^2)	2.2	1.3	4.0	1 41	2.0
Thermal power (MWt)	3600	3400	9300	4820	4000
Net plant efficiency	0.33	0.31	0.36	0.38	0.33
Net electric power (MWe)	1188	1054	3348	1832	1320

(ATF),[4] under construction at Oak Ridge National Laboratory (ORNL). The ATF configuration, a medium aspect ratio ($R/\bar{a} = 7$) torsatron with moderate rotational transform and shear, has the potential for high-beta operation due to magnetic self-stabilization (rapid increase in magnetic well depth with increasing beta) and elimination of the $q = 1$ surface from the plasma.

In addition to using a small plasma radius to increase the overall economic attractiveness of the Advanced Toroidal Facility Small Reactor (ATFSR), a small average radius ($\bar{a}$) plasma allows the impact of the radial electric field, created by the nonambipolar particle flux in a stellarator/torsatron, on plasma confinement to be readily observed. Prior stellarator/torsaron studies have only relied on the $(\bar{a})^2$ dependence of energy confinement to improve transport, neglecting the impact of the potentially large radial electric field.

Basic fusion reactor plasma power definitions and terminology, such as those used in Table I, are introduced in Chapter II. A plasma core power balance is described, along with the concept of ignited operation. Based on the desirability of a small power reactor as explained above and the plasma parameters determining the total thermal power and wall loading, the ATFSR average plasma radius is selected.

Chapter III outlines the ATF (ATFSR) magnetic configuration properties. After a review of fundamental particle motion in and geometry of a torsatron reactor, the equilibrium and stability properties of the ATF are explained, justifying the selection of an average beta of 9% for the ATFSR operating point.

Since the ATFSR average plasma radius has been selected in Chapter II and the magnetic coil configuration of the ATF described in Chapter III, Chapter IV details the ATFSR machine configuration properties based on a

scaled-up ATF design. The overall consistency of the ATFSR parameters and the machine configuration limitations are examined.

Chapter V contains a detailed review of particle orbits in a torsatron plasma and a description of the theory of neoclassical radial transport of particles, including the impact of a radial electric field. Chapter VI describes the fluid transport equations, which incorporate the particle and energy losses described in Chapter V. These equations are solved in the one-dimensional (1-D) WHIST transport code[5] for the ATFSR plasma.

Chapters VII and VIII describe the results of the ATFSR plasma analyses. Chapter VII shows the impact of the radial electric field on transport through the use of fixed profiles, whereas in Chapter VIII, the radial electric field is determined self-consistently.

Chapter IX covers the ATFSR ignited plasma parameters and power outputs and a comparison with prior stellarator/torsatron designs. Chapter X summarizes the results presented in the text and draws final conclusions.

CHAPTER II

FUSION REACTOR PLASMA POWER FUNDAMENTALS

At steady state, the alpha particle heating power (P_α) from the D-T fusion reaction

$$D + T \rightarrow {}_2^4He(3.52\ MeV) + n(14.1\ MeV) \tag{2-1}$$

plus the supplementary heating power (P_s) balance the transport power loss (P_{tr}) and the radiation power loss (P_{rad}),

$$P_\alpha + P_s = P_{tr} + P_{rad} \ . \tag{2-2}$$

The requirement for the plasma to achieve ignition is that the losses are sustained by alpha heating alone. Equation (2-2) represents a global steady-state power balance for the plasma. In Chapter VI, this analysis is expanded to include spatial variation, time dependence, particle and energy sources, etc.

The fusion power produced in a 50/50 D-T plasma is given by

$$P_f = n_i^2 \frac{\langle \sigma v \rangle_{DT}}{4} (17.62\ MeV) J V_p \quad (W) \ , \tag{2-3}$$

where n_i is the fuel ion density (m^{-3}), $\langle \sigma v \rangle_{DT}$ is the fusion reaction rate (m^3/s) averaged over a Maxwellian velocity distribution, J is 1.602×10^{-13}

joule/MeV, and V_p is the plasma volume (m^3). The alpha particle heating power is 3.52/17.62 of the fusion power.

Assuming that the plasma is Maxwellian, the average energy per particle is given by 1.5 kT, where k = 1.602×10^{-16} joule/keV is the Boltzmann constant and T is the particle's temperature in kiloelectron volts (keV). Therefore, the average energy densities of ions and electrons are 1.5 $n_i kT_i$ and 1.5 $n_e kT_e$. The transport power loss can be expressed as

$$P_{\text{tr}} = \frac{1.5\, n_i kT_i}{\tau_E^i} + \frac{1.5\, n_e kT_e}{\tau_E^e} \quad \text{(W)} \ , \tag{2-4}$$

where τ_E^i and τ_E^e are the energy confinement times (s) for ions and electrons, respectively.

In the absence of impurities, the radiation power loss is

$$P_{\text{rad}} = P_{\text{brems}} + P_{\text{syn}} \ , \tag{2-5}$$

where P_{brems} is bremsstrahlung radiation due to electron acceleration following collisions with ions and P_{syn} is synchrotron radiation due to electron acceleration from gyrations about magnetic field lines. An approximate expression for the bremsstrahlung radiation is[6]

$$P_{\text{brems}} \simeq n_e^2 (5 \times 10^{-37} Z_{eff}\, T_e^{1/2}) V_p \quad \text{(W)} \ , \tag{2-6}$$

where Z_{eff} is the effective atomic charge,

$$Z_{\text{eff}} = \frac{\sum_a n_a Z_a^2}{n_e} , \tag{2-7}$$

due to multiple ion species "a." For synchrotron radiation, an approximate expression is[6]

$$P_{\text{syn}} \simeq 6.21 \times 10^{-17} n_e T_e B^2 (1 + T_e/204) V_p (1-R)^{1/2} \quad \text{(W)} , \tag{2-8}$$

where B is the magnetic field strength [tesla (T)] and R is the fraction of synchrotron power reflected back into the plasma from the first wall.

Of the four power terms in Eq. (2-2), only the transport power loss is dependent upon a particular magnetic configuration. The alpha particle heating power, one-fifth of the D-T fusion power, the supplementary heating power (e.g., neutral-beam injection, radio-frequency heating), and the bremsstrahlung and synchrotron radiation powers are independent of machine design. The energy confinement times of the ions and the electrons ultimately determine the ability of a reactor to achieve the ignited state. Energy confinement is considered in more detail in Chapters V through VIII.

Even if the ignition condition is not met, the economic attractiveness of the reactor can be determined from the power amplification factor, defined as

$$Q = \frac{P_{\text{th}}}{P_s} , \tag{2-9}$$

where P_s is the supplementary heating power. For a D-T plasma, the total thermal power is

$$P_{\text{th}} = n_i^2 \frac{\langle \sigma v \rangle_{DT}}{4} Q_f J V_p \quad \text{(W)} \ , \tag{2-10}$$

for Q_f given by

$$Q_f = 3.52 + 14.1(1 + m_b)\,\text{MeV} \ , \tag{2-11}$$

where m_b is the blanket multiplication factor. This factor accounts for additional neutrons resulting from exothermic neutron reactions in the blanket material. The higher the value of Q for a given design, the better the overall economics of the system will be. A Q value greater than ten is generally accepted as sufficient for a power reactor, with a value of infinity indicating ignition.

The fusion power density, a measure of the fusion power per volume of the plasma core, is given by

$$FPD = P_f/V_p \quad (\text{W/m}^3) \ . \tag{2-12}$$

Likewise, the total thermal power density is given by

$$TPD = P_{\text{th}}/V_p \quad (\text{W/m}^3) \ . \tag{2-13}$$

Both the fusion power density and the total thermal power density indicate the degree of utilization of the plasma volume for power production in a specific reactor configuration. The higher the values of FPD and TPD for a given design, the more economic the production of electric power.

Beta, the ratio of plasma kinetic pressure to magnetic pressure, is given by

$$\beta = \frac{\sum_j n_j k T_j}{B^2/2\mu_0} \quad , \tag{2-14}$$

where n_j is the density of the j^{th} species (fuel ions, electrons, alpha particles, etc.), B is the magnetic field strength, and μ_0 is the permeability of free space. Assuming the kinetic pressure is due primarily to common temperature fuel ions, Eq. (2-14) may be rearranged for density and inserted into Eq. (2-10), yielding

$$P_{\text{th}} = \frac{\beta^2 B^4 <\sigma v>_{DT} Q_f J V_p}{16 \mu_0^2 T_i^2} \quad \text{(W)} \ . \tag{2-15}$$

The total thermal power may also be expressed in terms of neutron wall loading, P_w (W/m^2), such that

$$P_{\text{th}} = P_w S_w Q_f / Q_n \quad \text{(W)} \ , \tag{2-16}$$

where S_w is the first wall surface area (m^2) and Q_n is the neutron energy per D-T fusion (14.1 MeV). Rearranging Eq. (2-16) for P_w and inserting Eq. (2-15) for P_{th}, the neutron wall loading is given by

$$P_w = \frac{\beta^2 B^4 <\sigma v>_{DT} Q_n J V_p}{16 \mu_0^2 T_i^2 S_w} \quad (W/m^2) \ . \tag{2-17}$$

Equations (2-15) and (2-17) give insight into how plasma parameters interact with various technological and engineering constraints. The total thermal power output is to be maximized, while the neutron wall loading is kept to an acceptable level (from a first-wall lifetime consideration). The plasma beta and magnetic field strength values for an ATF-style magnetic configuration are discussed in detail in the next chapter. The maximum beta value depends upon stability and equilibrium limits intrinsic to the coil configuration. Likewise, the maximum field strength is limited by the maximum magnetic field tolerable at the inboard surface of a helical field coil.

The reactivity parameter, $<\sigma v>_{DT}/T_i^2$, exhibits a broad maximum from 8 to 25 keV.[7] The blanket multiplication factor m_b is between 0 and 0.5 for most blanket materials,[8] enabling the total thermal power to be increased up to 50% for a given set of plasma and machine parameters.

The plasma volume V_p is proportional to the square of the average plasma radius $\bar{a}$, and for a fitted first wall, the wall surface area S_w is directly proportional to $\bar{a}$. Therefore, exclusive of the maximum plasma beta and magnetic field strength values intrinsic to the ATF-style magnetic configuration, the only

plasma parameter variable in Eqs. (2-15) and (2-17) is the average plasma radius $\bar{a}$. Based on the discussion in Chapter I as to the desirability of a small, medium aspect ratio torsatron, an average plasma radius of 1 m is selected for the ATFSR.

CHAPTER III

ATFSR MAGNETIC CONFIGURATION PROPERTIES

A plasma cannot be contained in a finite aspect ratio toroidal magnetic field alone since the ions and electrons will experience a $\vec{B} \times \nabla B$ force, which leads to spatial charge separation. The resultant electric field will produce an $\vec{E} \times \vec{B}$ drift, causing losses of both ions and electrons. If a helical field component is added, the resultant magnetic field line will pass around the minor circumference of the torus while a trajectory is traced around the major circumference. Ions and electrons moving along the spiraling magnetic field lines will experience alternating $\vec{B} \times \nabla B$ forces, resulting in zero net charge separation.

In order to generate a closed magnetic surface in a torus, a given magnetic field line must not close upon itself after passing around the major circumference. The average poloidal angle ι between two successive intersections of a magnetic field line with a plane cutting the minor diameter of the torus is defined to be the rotational transform value in radians. Often ι is normalized by the one-turn toroidal angle, 2π, and written as $\dot{\iota}$. If $\dot{\iota}$ is a rational number, a closed magnetic line configuration results. Figure 1 illustrates the toroidal direction (ϕ), the poloidal direction (θ), and the poloidal angle change (ι) of a magnetic field line of an axisymmetric torus.

Since each field line creates its own magnetic surface, a set of nested toroidal surfaces result. The magnetic axis is the single field line about which all of the surfaces are nested.

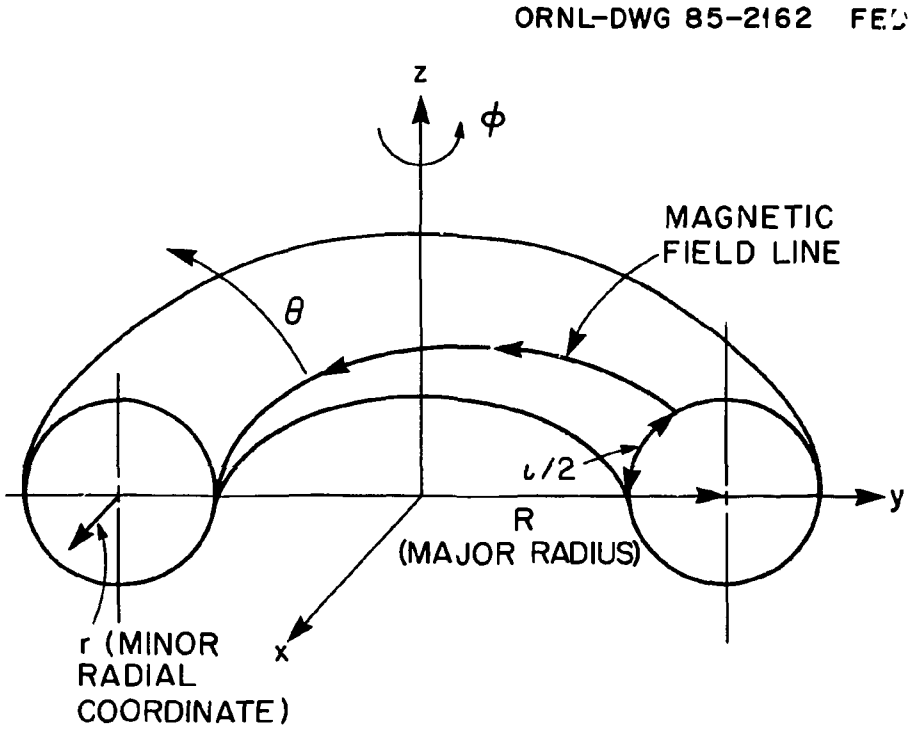

Fig. 1. Basic toroidal geometry. The geometry indicates toroidal direction (ϕ), poloidal direction (θ), one-half of poloidal angle change of a magnetic field line ($\iota/2$), major radius (R), and minor radial distance (r).

Torsatrons provide the helical twisting of the magnetic field lines by means of a set of helical coils. A single helical winding will provide toroidal, poloidal, and vertical field components. In a torsatron, the current in all of the helical conductors is in the same direction. The resultant twisting of the magnetic field lines is therefore in the same direction as the wrapping of the helical windings.

A torsatron magnetic configuration is set by the winding law chosen for the helical conductors. The ATF winding law[9] is

$$m\phi = \ell(\theta - \alpha \sin \theta) \ , \tag{3-1}$$

where ℓ is the poloidal harmonic number, m is the toroidal field period number, and α is the pitch modulation ($-1 < \alpha < 1$).

The poloidal harmonic number ℓ refers to the symmetry of the magnetic surfaces in the minor cross section and is the number of separate helical primary magnets. The toroidal field period number m is the number of times the symmetry of the magnetic surfaces in the minor cross section repeats in going once around the major circumference of the torus.

It is possible to modify the winding law of a torsatron by means of the pitch modulation α so that vertical field components are eliminated. Normally, as in the ATF, cancellation of the net vertical field is accomplished by adding separate vertical field coils. Figure 2 shows the complete continuous ATF coil set, with the last closed magnetic flux surface depicted inside the helical field coils. The ATF-style coil set consists of two ($\ell = 2$) unmodulated ($\alpha = 0$) torsatron windings with 12 toroidal field periods, 2 inner vertical field coils, and 2 outer vertical field coils. The currents in the inner vertical field coils flow in the

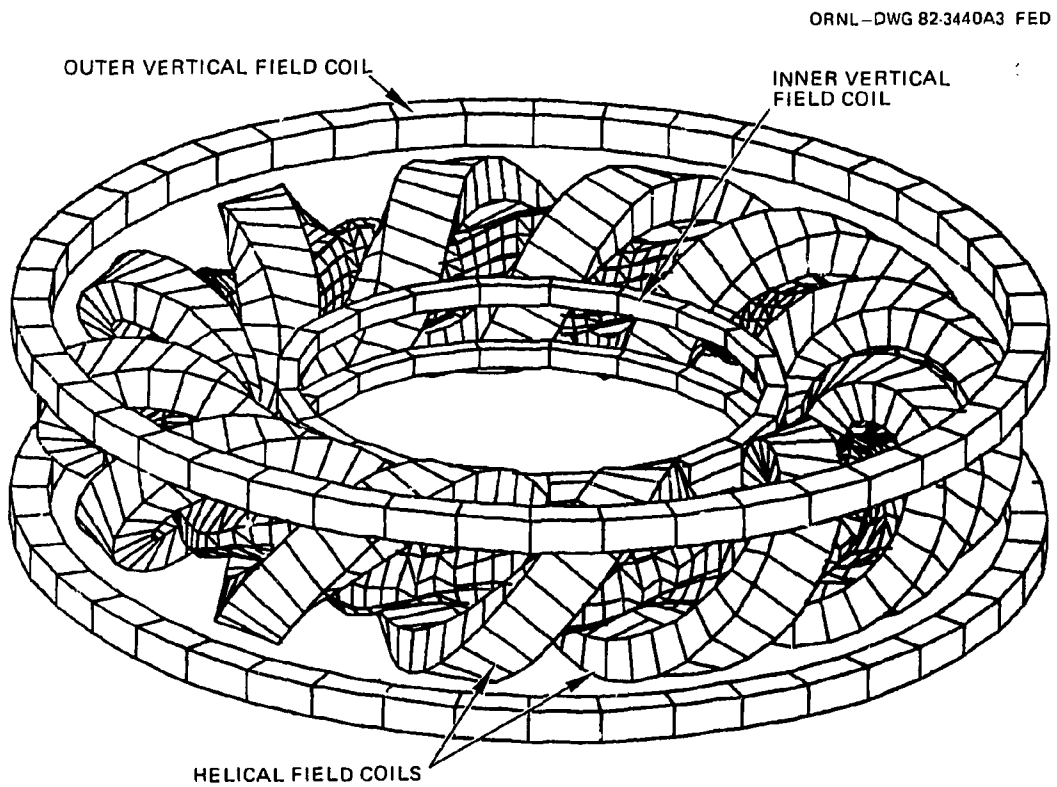

Fig. 2. The ATF-style coil set. The set shows the last closed flux surface inside the helical field coils. Both inner and outer vertical field coils are also shown.

same direction as the primary helical coils, while the currents in the outer set flow in the opposite direction.

The magnetic field strength near the magnetic axis is approximated[10] for the toroidal ATFSR by

$$B \simeq |B_\phi| \simeq B_0[1 - \epsilon_t \cos\theta - \epsilon_h \cos(\ell\theta - m\phi)] \ . \tag{3-2}$$

The toroidal modulation (ϵ_t) of the magnetic field is approximated by the inverse aspect ratio (r/R). The helical modulation (ϵ_h) of the magnetic field produced by the continuous helix is approximated by the parabolic equation

$$\epsilon_h = \epsilon_{h0} + \epsilon_{ha}\left(\frac{r}{\bar{a}}\right)^2 \ , \tag{3-3}$$

where ϵ_{h0} and ϵ_{ha} are the axial and edge values, respectively. For a torsatron, $\epsilon_h > \epsilon_t$. The ATFSR has a large helical field ripple, peaked at the plasma edge with a value of 22%. Figure 3 shows the helical magnetic ripple (%) as a function of minor radius. The helical modulation of the magnetic field is used in determining the transport coefficients of the helical trapping regime, as shown in Chapter V.

The magnetic configuration properties important for finite beta magneto-hydrodynamic (MHD) equilibrium and stability are the rotational transform profile and the specific magnetic volume profile.[11]

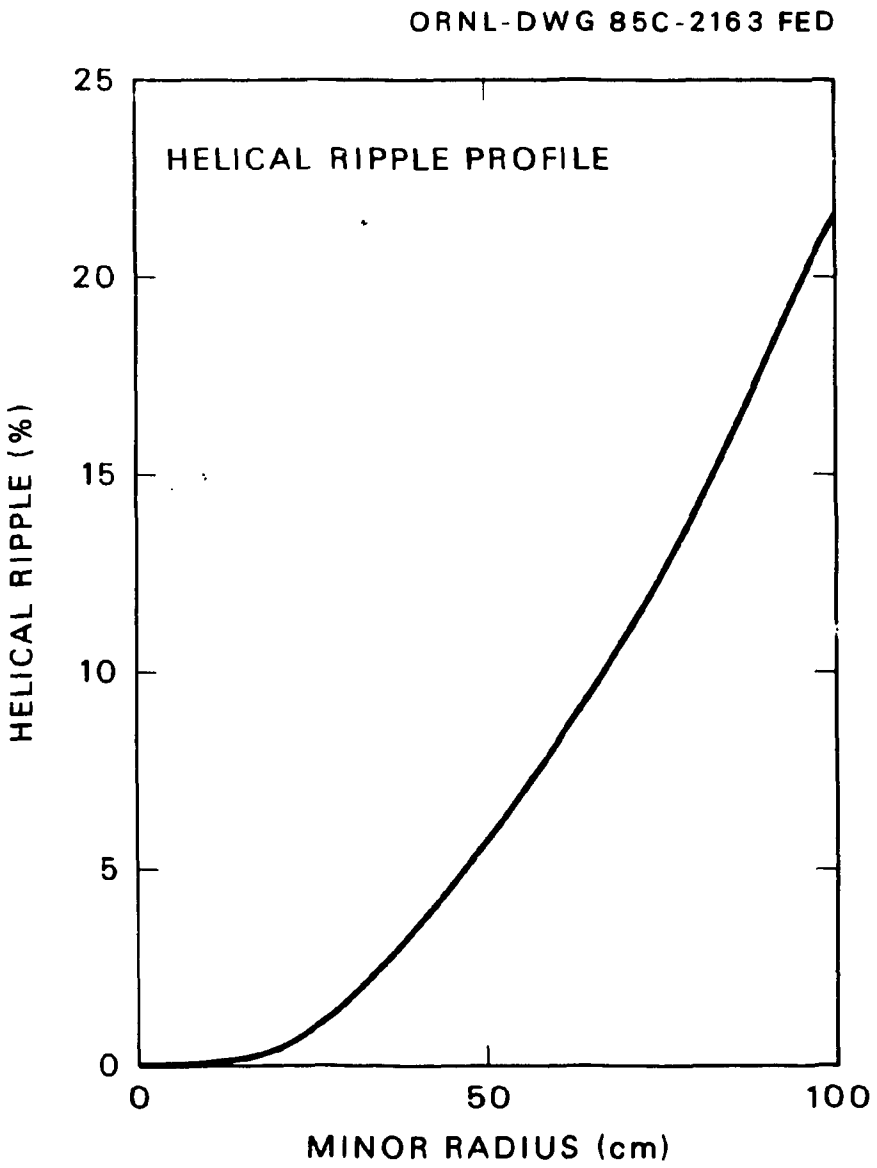

Fig. 3. The ATFSR helical magnetic ripple (%) as a function of minor radius.

The helical twist of the main coil set gives a rotational transform profile of moderate shear, $\dot{\iota}_a/\dot{\iota}_0$, with central transform $\dot{\iota}_0 = 0.35$ and edge transform $\dot{\iota}_a = 0.9$. The transform profile is approximated by

$$\dot{\iota}_a = \dot{\iota}_0 + (\dot{\iota}_a - \dot{\iota}_0)\left(\frac{r}{\bar{a}}\right)^2 \tag{3-4}$$

and is illustrated in Fig. 4 as a function of minor radius.

When plasma is created within the magnetic field and heating is begun, the plasma beta increases and a Pfirsch-Schlüter current begins flowing to balance the forces.[12] This current is obtained from the steady-state solution of the MHD equilibrium equations,

$$\nabla p = \vec{J} \times \vec{B} \ , \ \nabla \cdot \vec{J} = 0 \ . \tag{3-5}$$

The value of the Pfirsch-Schlüter current is approximated by

$$J_{PS} = \frac{4\pi}{\dot{\iota} B_0} \frac{\partial p}{\partial \rho} \cos\theta \ , \tag{3-6}$$

where p is the plasma pressure and ρ is the radial direction from the magnetic axis. Although the current does not have a net value, the flow generates a unidirectional vertical field across the plasma diameter, moving the magnetic axis outward. The vertical field coils can compensate for this outward motion during startup and move the magnetic axis back, enhancing the achievable equilibrium

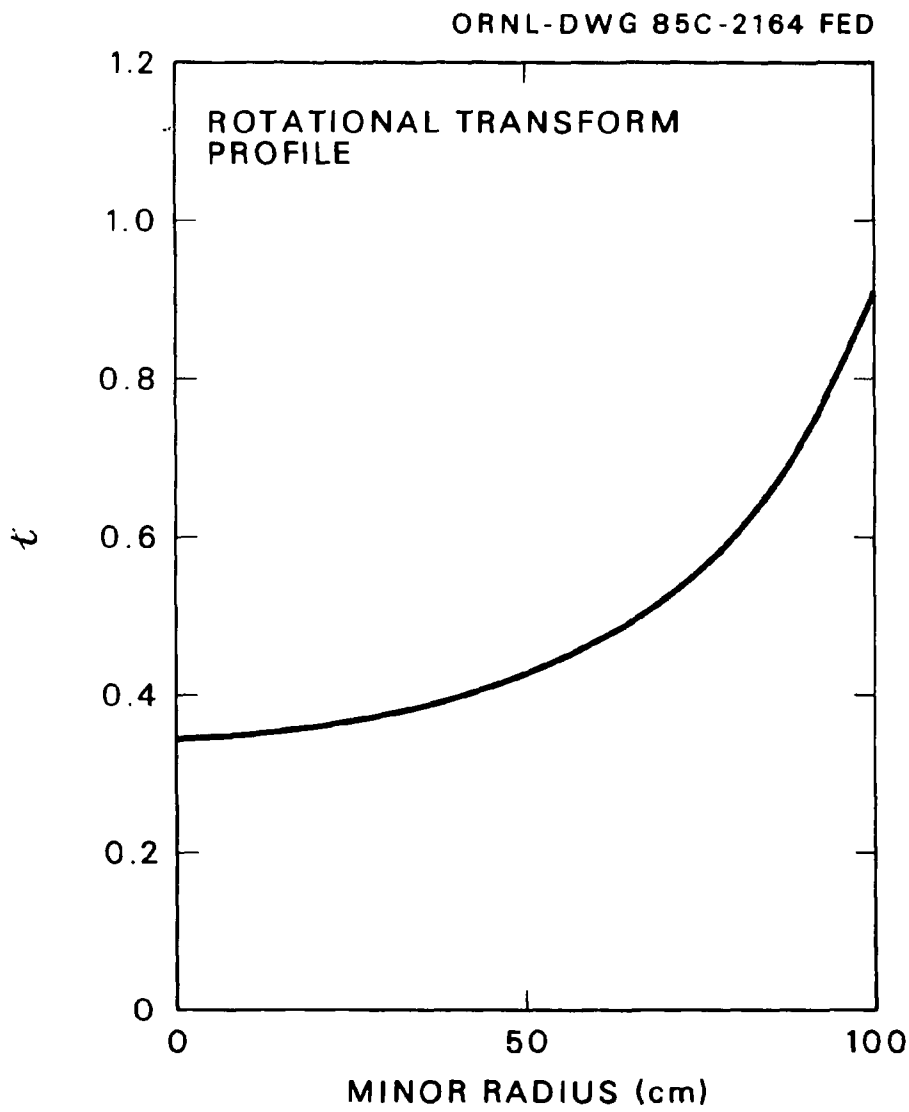

Fig. 4. The ATFSR rotational transform (ι) as a function of minor radius.

beta value. Likewise, the vertical field coils are employed in maintaining the vacuum rotational transform profile as beta is increased.

The specific magnetic volume[13] is defined as

$$V' = \lim_{N\to\infty} \frac{1}{N} \int_N \frac{d\ell}{B} \quad , \tag{3-7}$$

where N is the number of toroidal transits made by a field line. The ATF magnetic well depth,[14] defined as

$$\Delta V' = \frac{V'(0) - V'(\text{minimum})}{V'(0)} \quad , \tag{3-8}$$

is illustrated in Fig. 5 as a function of minor radius.

Noting that integral values of $q = 1/\iota$ lead to instabilities and loss of confinement, Fig. 4 indicates that $q = 1$ ($\iota = 1$) and $q = 3$ ($\iota = 0.33$) surfaces are located outside of the plasma. Comparing Figs. 4 and 5, the $q = 2$ surface is found to be in a region of low shear where $V'' < 0$, indicating interchange stability.

At ORNL, the finite beta properties of the ATF-style magnetic configuration have been extensively studied utilizing full three-dimensional (3-D) numerical techniques.[15] At a moderate plasma aspect ratio ($R/\bar{a}$) of 7 and coil aspect ratio ($R/\bar{a}_c$) of 4, the $m = 12$ ATF has no limitation due to low mode number, ideal MHD instabilities, and no equilibrium beta limit up to the resolution of the numerical techniques ($\langle\beta\rangle > 8\%$). Therefore, the ATF-style configuration is

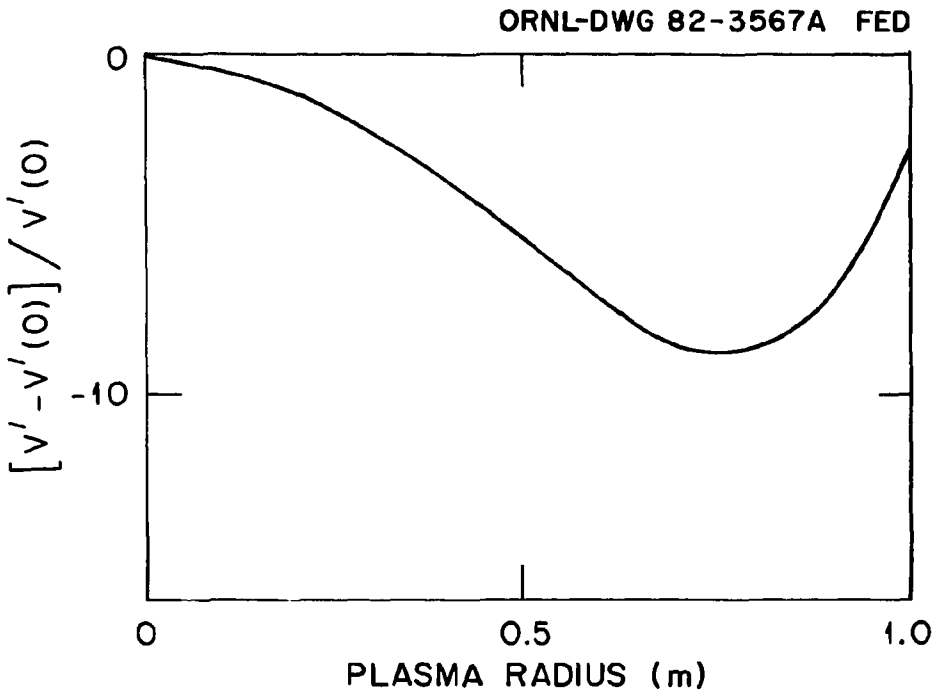

Fig. 5. The ATF magnetic well depth at $\langle\beta\rangle \sim 8\%$ as a function of minor radius.

able to achieve high stable beta values and enter a second stability region as shown in Fig. 6. The absence of a stability limit is due to the rapid deepening of the magnetic well as beta is increased (Fig. 5 shows the depth at $\langle\beta\rangle \sim 8\%$). The enhanced well produced by the self-stabilizing finite beta magnetic axis shift is sufficient to stabilize modes at $q = 2$, and since the $q = 1$ surface is excluded from the plasma, low mode number ideal instabilities are prevented from developing in the $V'' > 0$ edge region. Therefore, the maximum achievable $\langle\beta\rangle$ of the ATF-style configuration is determined by equilibrium, rather than stability, considerations. The finite beta magnetic axis shift can be kept small enough not to limit equilibrium beta but large enough to allow proper magnetic well depth by use of the vertical field coils.

The magnetic configuration properties and coil design of the ATF are assumed similar for the ATFSR. Operation of the ATFSR at $\langle\beta\rangle = 9\%$ is chosen in Chapter IX since this value is near the resolution limit of the numerical techniques, but not necessarily of the ATF magnetic configuration itself, which may be capable of attaining considerably higher beta values.

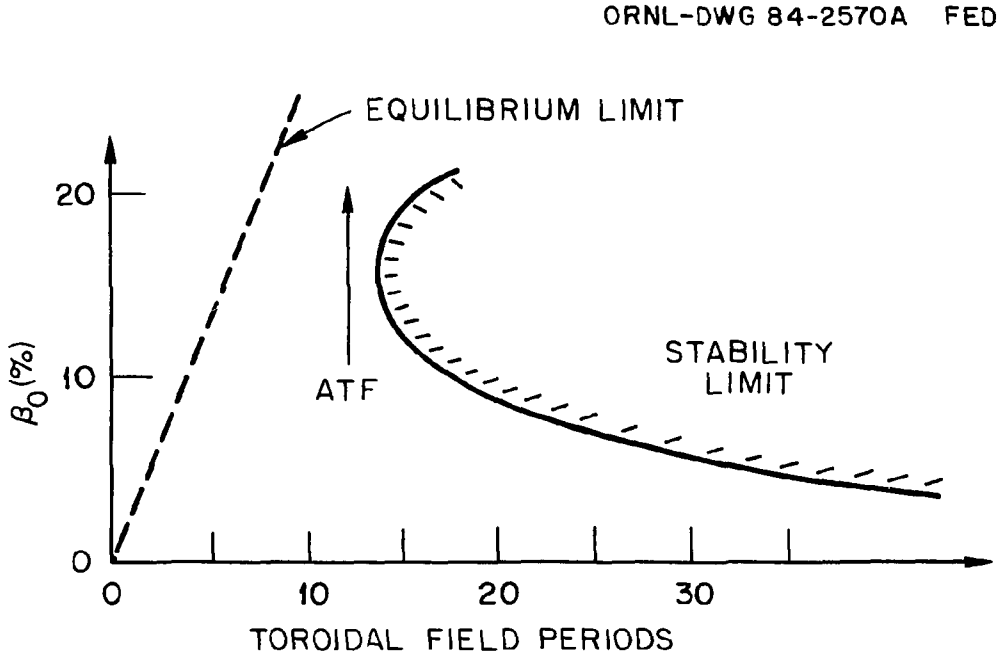

Fig. 6. Combined equilibrium and stability constraints for ATF (ATFSR) illustrated as central beta (β_0) as a function of toroidal field period number (m). These constraints indicate possible access to second stability region at $m = 12$.

CHAPTER IV

ATFSR MACHINE CONFIGURATION PROPERTIES

It is essential in the study of fusion plasmas to be concerned not only with a knowledge of the physics that defines the plasma parameters but also with a knowledge of how the plasma parameters interact with various technological and engineering constraints.

In Chapter II, an average plasma radius $\bar{a}$ of 1 m was chosen for the ATFSR. As described in Chapter III, the ATF has 12 toroidal field periods, a multipolarity of 2, a plasma aspect ratio of 7, and a coil aspect ratio of 4. The ratio of the maximum magnetic field at the coil to the central magnetic field is approximately two for the ATF coil configuration.[16] Utilizing a rectangular approximation, the ATF coil is 0.5 m wide by 0.25 m thick. The resistive coil's current density is 28.2 MA/m^2, with a current of 1.76 MA per coil. In order to determine the ATFSR machine dimensions, the ATF magnetic configuration is scaled-up, maintaining the ATF plasma and coil aspect ratios along with the ratio of the coil width to the coil thickness.

The ATFSR has a major radius of 7 m based upon the choice of $\bar{a} =$ 1 m and the required plasma aspect ratio ($R/\bar{a}$) of 7. With a coil aspect ratio ($R/\bar{a}_c$) of 4, the average coil radius (the average radial distance from the center of the plasma to the center of the coil) is 1.75 m. A plasma elongation (b_p/a_p, where a_p is the semiminor radius and b_p is the semimajor radius) of 1.65 is typical of the $\ell = 2$ harmonic elliptic shape. Since πab is the area of an ellipse and $\pi(\bar{a})^2$ the equivalent area of a circle, the semiminor radius is 0.78 m and

the semimajor radius is 1.29 m. Assuming the first wall is a distance 10% of the semiminor radius from the plasma, the semiminor wall radius a_w is 0.86 m and the semimajor wall radius b_w is 1.37 m.

The maximum field that can bc produced at the coil depends on its conductor type and its specific design. Since large dissipative power losses would result from using resistive ATF-style coils, a superconducting coil system is used in ATFSR, exhibiting essentially no electrical resistance. A choice of an on-axis magnetic field strength of 5 T would result in a maximum field at the coil of -10 T, based upon the one-to-two ratio of the ATF-style helical coil. A modest value of 10 T at the coil would allow for either NbTi or a NbTi and Nb_3Sn combination to be used as the superconducting portion of the winding in the coils.[17] As will be shown in Chapter VIII, plasma confinement is only slightly enhanced by selection of a significantly higher on-axis magnetic field strength of 7 T. The resulting value of 14 T at the coil would require materials and design techniques beyond near-term technology capabilities.

The coil thickness is given by

$$\delta_{CT} = \left[\frac{2\pi R B_o}{\mu_o m J f \cdot 10^6}\right]^{1/2} \text{(m)} , \tag{4-1}$$

where B_o is the on-axis magnetic field in tesla, μ_o is the permeability of free space, m is the number of complete poloidal wrappings of the torus by both coils, J is the average current density (MA/m^2) of the winding, and f is the ratio of the coil width to the coil thickness. Using an average current density over the winding of 15.0 MA/m^2, typical of NbTi in a copper matrix,[18] in Eq.

(4-1) yields a coil thickness δ_{CT} of 0.7 m and a coil width δ_{CW} of 1.4 m. With a first-wall thickness of 0.05 m and a uniform coil dewar of 0.1 m, the coil shield thickness ΔS is approximately 0.4 m. Tungsten (W) with boron carbide (B_4C) has been found to be a suitable material for space-restricted shield applications in previous detailed neutronic analyses,[19] although at a greater thickness of 0.6–0.7 m. A detailed thermal-hydraulic and shielding analysis is required to verify adequate coil protection. If inadequate, the coil aspect ratio may be reduced slightly to allow for more coil shield, as long as the increased maximum field at the coil is acceptable. Substantial space exists between the helical coils for the tritium breeding blanket and associated shield. Figure 7 shows a blanket-shield thickness ΔBS of 1.5 m between the coils, which is variable as space allows as the helical coils rotate through a field period.

All ATFSR magnet and machine parameters are summarized in Tables II and III, respectively. Figure 7 shows a cross-section view of the ATFSR. With the possible exception of coil shield thickness, all parameters and dimensions listed in these tables and shown in the figure indicate that the ATFSR machine configuration is both self-consistent and technologically feasible.

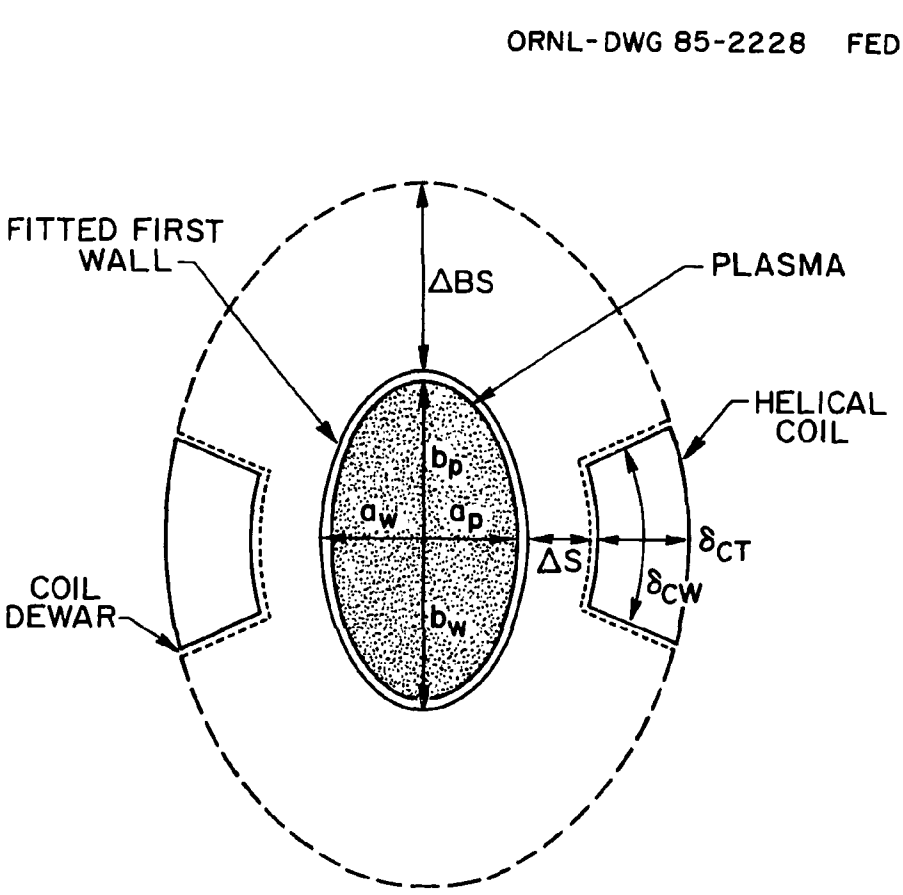

Fig. 7. Cross section view of the ATFSR. Illustrated are the elliptic plasma (semiminor radius a_p, semimajor radius b_p) with a fitted first wall (semiminor wall radius a_w, semimajor wall radius b_w), the coil shield thickness ΔS and the blanket-shield thickness ΔBS, the coil dewars, and the helical coils (coil thickness δ_{CT}, coil width δ_{CW}). The vacuum chamber rotates poloidally with toroidal field period number $m = 12$.

Table II. ATFSR Magnet Parameters

Coil configuration	continuous
Number of coils, N	2
Multipolarity, ℓ	2
Number of toroidal total field periods, m	12
Coil aspect ratio, A_c	4.0
Iota-bar on axis, ι_0	0.35
Iota-bar at edge, ι_a	0.90
On-axis magnetic field strength, B_o	5.0 T
Maximum magnetic field at conductor, B_{max}	10.0 T
Conductor current in each coil, I_c	7.35 MA
Conductor current density, J	15.0 MA/m^2
Coil conductor thickness, δ_{CT}	0.7 m
Coil conductor width, δ_{CW}	1.4 m
Coil conductor cross-sectional area	0.98 m^2
Dewar thickness	0.1 m
Total coil cross-sectional area	1.44 m^2

Table III. ATFSR Machine Parameters

First-wall configuration	fitted
Wall semiminor radius, a_w	0.86 m
Wall semimajor radius, b_w	1.37 m
Wall surface area, S_w	276.3 m^2
First-wall thickness, ΔFW	0.05 m
Coil shield thickness, ΔS	0.4 m
Blanket-shield thickness, ΔBS	1.5 m

CHAPTER V

TORSATRON PARTICLE ORBITS AND TRANSPORT THEORY

The helical field lines in a torsatron plasma guide charged particles as described in Chapter III. Without collisions, a charged particle's motion is therefore confined to a flux surface, except for ∇B and toroidal curvature drifts. Over a particle's complete orbit, the net radial displacement is zero. On a particular flux surface, the plasma density, temperature, and pressure may be considered constant.

As a charged particle spirals along a magnetic field line, both kinetic energy and magnetic moment are conserved:[20]

$$W = \frac{1}{2} m v^2 = \frac{1}{2} m(v_\parallel^2 + v_\perp^2) = \text{constant} \ , \tag{5-1}$$

$$\mu = \frac{m v_\perp^2/2}{B} = \text{constant} \ , \tag{5-2}$$

where m is the particle mass, $v_\parallel$ is the velocity component parallel to the field line, and $v_\perp$ is the velocity component perpendicular to the field line.

In a torsatron, three general classes of particle orbits exist: circulating, toroidally trapped, and helically trapped.[21] Circulating, or untrapped, particles travel completely around the torus without being reflected at any point along their field line. The maximum magnetic field encountered in traversing the torus is at the inside edge, denoted B_{max}. Combining Eqs. (5-1) and (5-2) yields

$$v_{\parallel} = \left[\frac{2}{m}(E - \mu B)\right]^{1/2} . \tag{5-3}$$

For a circulating particle, $E > \mu B_{max}$. However, for a toroidally trapped particle, $E < \mu B_{max}$, with the parallel velocity vanishing in the region of increasing magnetic field, reflecting the particle back. As the trapped particle guiding center bounces back and forth along the field line, it experiences a vertical drift due to ∇B and toroidal curvature drifts. This drift gives the trapped particle orbits their characteristic banana shape.

Helically trapped particles reflect on the local mirrors of the helical field, becoming trapped in the helical ripples. Due to ∇B and curvature drifts, helically trapped particles also have banana-shaped orbits. Unless a collision occurs or the helically trapped particle also becomes trapped in the toroidal field, the center of the helical banana orbit moves in a circle about the magnetic axis. A superbanana orbit may occur if a helically trapped particle also becomes toroidally trapped.

The origins and orbit characteristics of these types of particles are illustrated in Figs. 8 and 9. Figure 8 shows the field strength modulations along a magnetic field line due to toroidal and helical field components, creating banana, helical banana, and superbanana orbits. Details of these orbits are illustrated in Fig. 9.

In neoclassical theory, there are various transport regimes depending on the relative values of the collision frequency, mirror reflection (bounce) frequency, and the presence of an electric field. Since radial motion is diffusive, it may be characterized by a diffusion coefficient:[22]

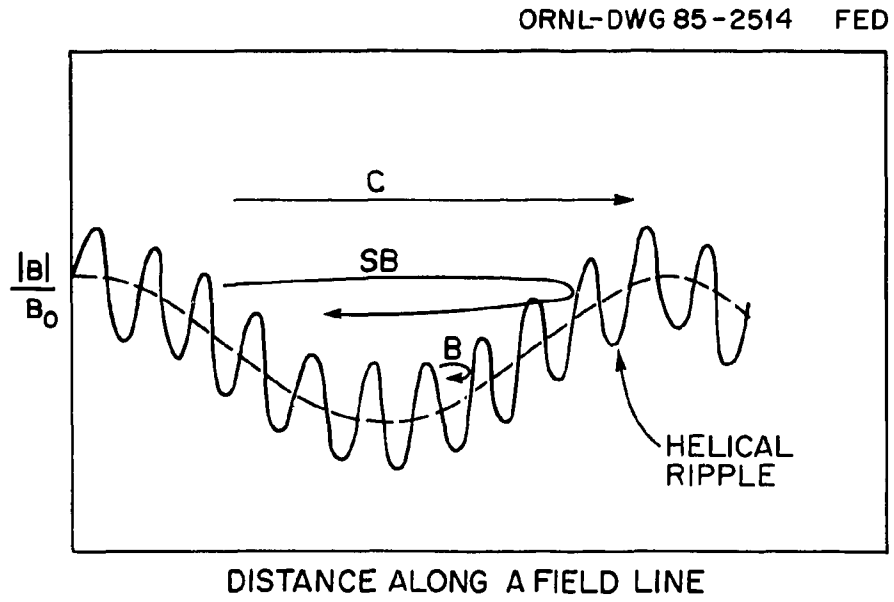

Fig. 8. Magnetic field strength modulations (magnitude of magnetic field over the central magnetic field) along a field line due to toroidal and helical field components. (C indicates a circulating particle; B indicates the banana orbit of a helically trapped particle; SB indicates a superbanana orbit.)

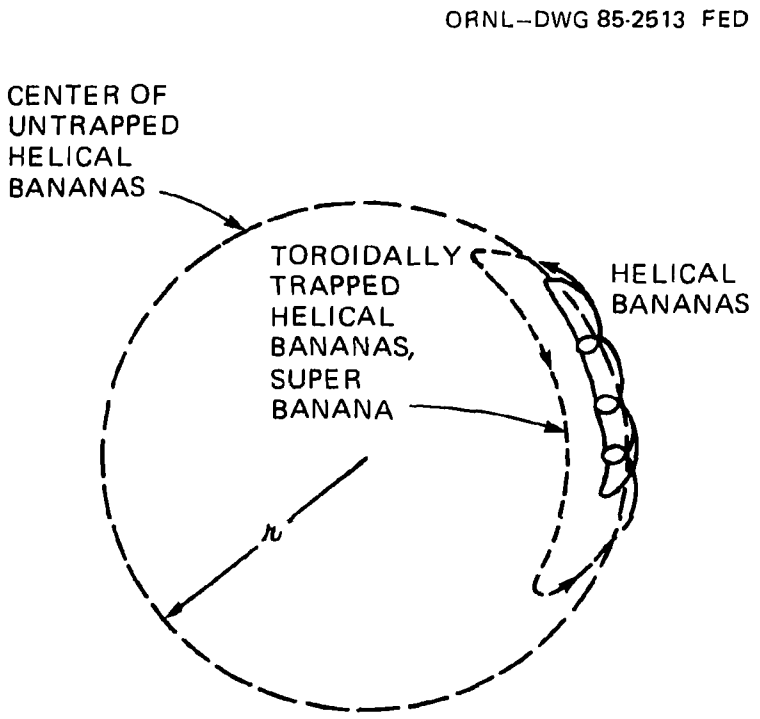

Fig. 9. Qualitative illustration of helical banana and superbanana particle orbits projected onto a constant ϕ plane. (r is the radial distance from the center of the orbits of the the untrapped helical bananas to the magnetic axis).

$$D \simeq f \frac{(\Delta r)^2}{\tau} = f(\Delta r)^2 \nu_{\text{eff}} \quad (\text{m}^2/\text{s}) \ , \tag{5-4}$$

where Δr (m) is the displacement of a particle from a magnetic surface in an average effective scattering time τ (s), ν_{eff} (s^{-1}) is the effective collision frequency, and f is the fraction of particles contributing to the diffusion process.

In the low-temperature collisional regime, neoclassical diffusion processes are identical to those derived in axisymmetric tokamak transport analyses:[23]

$$D_{\text{PS}} \simeq \nu_e \rho_e^2 q^2 - \text{Pfirsch-Schlüter (collisional)} \ , \tag{5-5}$$

$$D_p \simeq (\text{v}_{th_e}/qR)\, \rho_e^2 q^2 - \text{plateau (transitional)} \ , \tag{5-6}$$

where ν_e is the electron collision frequency for 90° scattering,[24] ρ_e is the electron gyroradius, and v_{th_e} is the electron thermal velocity. The transition between the two regimes occurs when $\nu_e = \omega_p \simeq \text{v}_{th_e}/qR$. The electron collision frequency, gyroradius, and thermal velocity are given by

$$\nu_e = \nu_{ee} + \nu_{ei} \ , \tag{5-7}$$

$$\rho_e = \frac{(2 m_e T_e)^{1/2}}{e B} \ , \tag{5-8}$$

$$\text{v}_{th_e} = \left[\frac{T_e}{m_e}\right]^{1/2} \ , \tag{5-9}$$

where ν_{ee} is the electron-electron collision frequency, ν_{ei} is the electron-ion collision frequency, e is unit charge, m_e is electron mass, and T_e is electron temperature.

As the plasma temperature increases, the low collisionality regime is entered. Helical trapping occurs but collisions are still frequent enough such that complete precession around the magnetic axis cannot occur. The ∇B drift effect is not completely canceled. The helically trapped diffusion coefficient D_h increases with decreasing collision frequency. The diffusion step size is

$$\Delta r_h \simeq \frac{v_{\nabla B}}{\nu_e} \epsilon_h \ . \tag{5-10}$$

The fraction of helically trapped particles is $\sqrt{\epsilon_h}$:

$$D_h \simeq \sqrt{\epsilon_h} \left(\frac{v_{\nabla B}}{\nu_e} \epsilon_h \right)^2 \frac{\nu_e}{\epsilon_h} = \epsilon_h^{3/2} \frac{v_{\nabla B}^2}{\nu_e} = \epsilon_h^{3/2} \left(\frac{T}{eBR} \right)^2 \nu_e^{-1} \ . \tag{5-11}$$

The helical trapping region is known as the $1/\nu$ regime.[25] This region is entered when the collision frequency is less than the helical bounce frequency,

$$\omega_{hb} \simeq \frac{v_{th}}{qR} \epsilon_h^{3/2} \ . \tag{5-12}$$

Assuming that the electric field, $E_r = -\nabla\phi$, is very small at a particular region in the plasma, when the collision frequency is less than the circulating

banana poloidal drift frequency, the helical plateau regime is entered.[26] The circulating banana drift frequency is

$$\omega_{cb} \simeq \frac{T}{eBr^2}\,\epsilon_h^2 \ . \tag{5-13}$$

The helical plateau diffusion coefficient D_{hp} is

$$D_{hp} \simeq \frac{\epsilon_t^2}{\sqrt{\epsilon_h}}\,\frac{T}{eB} \tag{5-14}$$

and is independent of collision frequency.

Assuming that the electric field is still very small, a further increase in plasma temperature, and subsequent decrease in collisionality below the superbanana poloidal drift frequency, results in formation of superbanana orbits.[27] The diffusion step size is

$$\Delta r_{sb} \simeq \left(\frac{\epsilon_t}{\epsilon_h}\right)^{1/2} r \ . \tag{5-15}$$

The fraction of particles both helically and toroidally trapped is $\sqrt{\epsilon_t}$. Therefore,

$$D_{sb} \simeq \sqrt{\epsilon_t}\left[\left(\frac{\epsilon_t}{\epsilon_h}\right)^{1/2} r\right]^2 \frac{\nu_e}{\epsilon_t} = \frac{\epsilon_t^{1/2}}{\epsilon_h}\, r^2 \nu_e \ , \tag{5-16}$$

effective when the collisionality is less than

$$\omega_{sb} \simeq \frac{T}{eBr^2}\,\epsilon_h^{1/2}\,\epsilon_t^{3/2} \quad . \tag{5-17}$$

The dependence of the diffusion coefficient D on ν_e is shown in Fig. 10. In the absence of an electric field, plasma confinement at low collisionality would be poor. In a stellarator/torsatron, however, the particle fluxes are not intrinsically ambipolar due to an imbalance in the electron and ion particle fluxes from helical ripple. A radial electric field E_r develops to ensure quasi-neutrality.[28] This electric field is effective in reducing losses since the radial drift velocities of helically trapped particles are slow compared to the $\vec{E} \times \vec{B}$ poloidal velocity, even for small radial potentials.[29]

The collisionless detrapping regime is entered when the collisionality is less than

$$\omega_{dt} \simeq \frac{E_r}{eBr}\,\epsilon_h \quad . \tag{5-18}$$

The collisionless detrapping diffusion coefficient[30] D_E is

$$D_E \simeq \frac{\epsilon_h^{1/2}}{\epsilon_t}\left(\frac{T}{eBR}\right)^2 \frac{\nu_e}{\omega_E^2} \tag{5-19}$$

where ω_E is the $\vec{E} \times \vec{B}$ drift frequency,

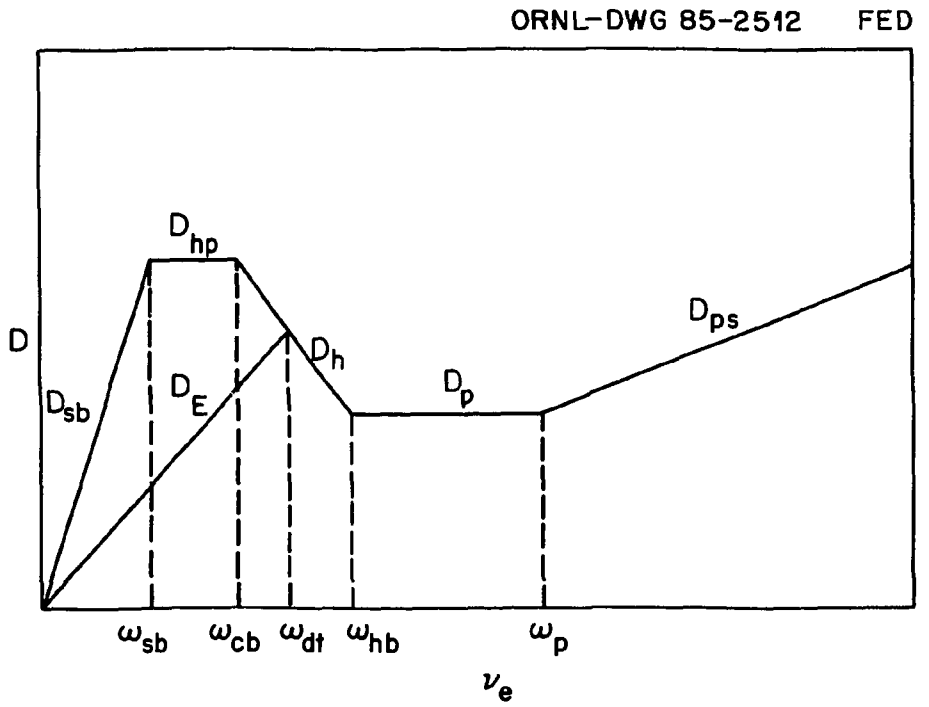

Fig. 10. Particle diffusion coefficient D versus electron collision frequency ν_e. Illustrated are the Pfirsch-Schlüter (PS), plateau (P), helically trapped (H), helical plateau (HP), superbanana (SB), and collisionless detrapping (E) regimes. Transition frequencies between Pfirsch-Schlüter and plateau regimes (ω_p), plateau and helically trapped regimes (ω_{hb}), helically trapped and helical plateau regimes (ω_{cb}), helical plateau and superbanana regimes (ω_{sb}), and helically trapped and collisionless detrapping regimes (ω_{dt}) are also shown.

$$\omega_E = \frac{E_r}{eBr} \quad . \tag{5-20}$$

The collisionless detrapping regime is smoothly joined with the helical trapping region in a model described in Chapter VI.

CHAPTER VI

PARTICLE AND ENERGY TRANSPORT EQUATIONS

Due to the very fast flow of particles and energy along helical field lines, densities, temperatures, and electric potential are considered constant on a flux surface. In a closed magnetic field configuration, particles and energy escape from the plasma by transport from one magnetic flux surface to another. This cross-field radial transport is driven by density, temperature, and electrostatic potential gradients found within the plasma.

The radial diffusion of particles and energy, as described in Chapter V, along with the electric field evolution, is modeled with a one-dimensional (1-D) transport code, WHIST.[31] The WHIST code treats a torsatron plasma as a circular cylinder (spatial dependence in the ρ coordinate).

Basic particle and energy transport cquations are found by taking velocity moments of the Boltzmann equation. Averaging the particle, momentum, and energy moments over a magnetic flux surface removes two of the spatial dimensions and thus yields a set of fluid equations with 1-D spatial variation.[32]

The transport equation for particles is

$$\frac{\partial}{\partial t} n_a + \frac{1}{V'(\rho)} \frac{\partial}{\partial \rho} [V'(\rho)\Gamma_a] = S_{p_a} \tag{6-1}$$

for each of the thermal species' densities n_a. Γ_a is the total particle flux of species "a," ions or electrons. S_{p_a} is the source of particles of type "a." Particle sources are gas puffing, pellet injection, and fusion reactions.

Electrons are subject to charge neutrality and ambipolar diffusion constraints:

$$n_e = \sum_a Z_a n_i \tag{6-2}$$

and

$$\Gamma_e = \sum_a Z_a \Gamma_i \ , \tag{6-3}$$

where Z_a = charge number of the ath ion species. The radial electric field, $E_r = -\nabla\phi$, is determined using the ambipolarity equation.

The transport equations for energy are

$$\frac{3}{2}\frac{\partial}{\partial t}\left[\left(\sum_a n_a\right)T_i\right] + \sum_a \left\{\frac{1}{V'(\rho)}\frac{\partial}{\partial \rho}\left[V'(\rho)\left(q_a + \frac{5}{2}\Gamma_a T_i\right)\right]\right\}$$

$$= \sum_a \left[\frac{\Gamma_e}{n_e}\frac{\partial}{\partial \rho}(n_a T_i) + Q_{ea} + S_{Ea} - Z_a \Gamma_a \phi'\right] \tag{6-4}$$

for thermal ions of species "a" and

$$\frac{3}{2}\frac{\partial}{\partial t}(n_e T_e) + \frac{1}{V'(\rho)}\frac{\partial}{\partial \rho}\left[V'(\rho)\left(q_e + \frac{5}{2}\Gamma_e T_e\right)\right]$$

$$= -\sum_a \left[\frac{\Gamma_e}{n_e}\frac{\partial}{\partial \rho}(n_a T_i) + Q_{ea}\right] + S_{Ee} + \Gamma_e \phi' \tag{6-5}$$

for thermal electrons.

Each of the terms in the preceding equations are functions of the effective radial coordinate ρ, which indicates the distance to the flux surface ψ from the plasma center at the midplane. V denotes the plasma volume within a flux surface, with V' indicating the surface area:

$$V' = 2\pi \oint \frac{d\ell}{B} \quad , \tag{6-6}$$

where $d\ell$ = differential field line length. Therefore, the total number of species "a" ions flowing across the surface at ρ per unit time is $V'(\rho)\Gamma_a$.

All ion species are assumed to have a common Maxwellian temperature T_i, with the electrons having Maxwellian temperature T_e. The conduction (random) heat flux is represented by q, and $5/2\Gamma T$ is the convection heat flux. The first term on the right-hand sides of Eqs. (6-4) and (6-5) is a flow-work term, while Q_{ea} is the rethermalization term. The last terms involving ϕ' are electric field work terms. For ion energy sources (losses) S_{Ei}, radio-frequency heating and charge exchange are used. For electron energy sources (losses) S_{Ee}, radio-frequency heating and radiation are used.

The transport equations are solved numerically in WHIST by employing the finite difference method to approximate the derivatives. The noncircular flux surfaces of the $\ell = 2$ ATFSR are modeled as equivalent circles, conserving area and volume. The finite difference equations are solved using a fully implicit scheme.[33] Time step sizes are internally chosen by WHIST such that densities and temperatures do not change excessively over a time step.

The total particle and heat flux terms can be expressed in terms of a general set of particle and heat transport coefficients which are divided into nonambipolar (*na*) contributions from the helical ripple plus contributions from nonhelically trapped particles and anomalous transport processes:

$$\Gamma_a = \Gamma_a^{na} - \sum_{a'} D_{aa'}^n \frac{\partial n_{a'}}{\partial \rho} - D_{ai}^T \frac{\partial T_i}{\partial \rho} - D_{ae}^T \frac{\partial T_e}{\partial \rho} - D_a^\phi \frac{\partial \phi}{\partial \rho} \tag{6-7}$$

and

$$Q_a = Q_a^{na} - \sum_{a'} n_a \chi_{aa'}^n \frac{\partial n_{a'}}{\partial \rho} - n_a \chi_{ai}^T \frac{\partial T_i}{\partial \rho} - n_a \chi_{ae}^T \frac{\partial T_e}{\partial \rho} - n_a \chi_a^\phi \frac{\partial \phi}{\partial \rho} \tag{6-8}$$

where χ (m^2/s) is the heat conductivity and Q_a = total heat flow = q_a + 5/2 $\Gamma_a T_a$ for species "a," ions or electrons. The superscripts on the Ds and χs refer to the density gradient (n), the temperature gradient (T), and the electrostatic potential gradient (ϕ). The nonhelically trapped contributions in Eqs. (6–7) and (6–8) are usually simplified by assuming that the diagonal terms are dominant, such that

$$\Gamma_a \simeq \Gamma_a^{na} - D_{aa}^n \frac{\partial n_a}{\partial \rho} \ , \tag{6-9}$$

$$Q_i \simeq Q_i^{na} - n_i \chi_{ii}^T \frac{\partial T_i}{\partial \rho} \ , \tag{6-10}$$

and

$$Q_e \simeq Q_e^{na} - n_e \chi_{ee}^T \frac{\partial T_e}{\partial \rho} \quad . \tag{6-11}$$

As described in Chapter VII, these diagonal particle diffusion and heat conductivity coefficients are divided into axisymmetric neoclassical and anomalous contributions, with the anomalous terms used for simulating experimental observations of transport more accurately.

In order to model the nonambipolar fluxes due to helical trapping, the particle and heat fluxes in the presence of an electric field in the $1/\nu$ and ν regimes have been derived,[34] and these regimes smoothly joined together at the resonant transition where $\vec{E} \times \vec{B}$ and $\vec{B} \times \nabla B$ drifts cancel. The resulting expression for the nonambipolar particle flux due to helical trapping is

$$\Gamma_a^{na} = -\epsilon_t^2 \epsilon_h^{1/2} \nu_{da}^2 n_a \int_0^\infty dx\, x^{5/2} e^{-x} \tilde{\nu}_a(x) \frac{A_a(x)}{\omega_a^2(x)} \tag{6-12}$$

and that for the nonambipolar total heat flux

$$\begin{aligned} Q_a^{na} &= q_a^{na} + \frac{5}{2} \Gamma_a^{na} T_a \\ &= -\epsilon_t^2 \epsilon_h^{1/2} \nu_{da}^2 n_a T_a^2 \int_0^\infty dx\, x^{7/2} e^{-x} \tilde{\nu}_a(x) \frac{A_a(x)}{\omega_a^2(x)} \quad . \end{aligned} \tag{6-13}$$

These equations are valid for $\epsilon_h > \epsilon_t$ and for the magnetic field approximation [Eq. (3-2)]. In these expressions,[35]

$$v_{da} = \frac{T_a}{Z_a e B r} \quad , \tag{6-14}$$

$$\tilde{\nu}_a(x) = \frac{\nu_a(x)}{\epsilon_h} \quad , \tag{6-15}$$

$$x = \frac{m_a v_{th_a}^2}{2 T_a} \quad , \tag{6-16}$$

$$A_a(x) = \frac{1}{n_a} \frac{\partial n_a}{\partial \rho} + \frac{Z_a e}{T_a} \frac{\partial \phi}{\partial \rho} + \left[x - \frac{3}{2}\right] \frac{\partial T_a}{\partial \rho} \frac{1}{T_a} \quad , \tag{6-17}$$

$$\omega_a^2 = \omega_d^2 + \omega_s^2 + \omega_p^2 + \omega_\nu^2 \quad , \tag{6-18}$$

$$\omega_d^2 = 1.67 \frac{\epsilon_t}{\epsilon_h} (\omega_E + \omega_{\nabla B_a})^2 \quad , \tag{6-19}$$

$$\omega_s^2 = 0.25 \left[\frac{\epsilon_t}{\epsilon_h}\right]^{3/2} \omega_{\nabla B_a}^2 \quad , \tag{6-20}$$

$$\omega_p^2 = 0.6 |\omega_{\nabla B_a}| \frac{\nu_a(x)}{\epsilon_h} \quad , \tag{6-21}$$

$$\omega_\nu^2 = 3.0 \left[\frac{\nu_a(x)}{\epsilon_h}\right]^2 \quad , \tag{6-22}$$

$$\omega_{\nabla B_a} = -v_{da} \frac{\partial \epsilon_h}{\partial \rho} x \quad , \tag{6-23}$$

where v_{da} is the drift velocity of species "a," Eqs. (6-19) through (6-22) are the contributions, respectively, from the nonresonant collisionless detrapping regime ($\sim\nu$), the resonant superbanana regime, the resonant superbanana plateau regime, and the $1/\nu$ collisional regime, and $\omega_{\nabla B_a}$ is the ∇B drift frequency of species "a."

The dominant frequency in ω_a^2, Eq. (6-18), determines the collisionality regime of a particle with energy x, Eq. (6-16). If ω_ν^2 is the largest term in ω_a^2, the particle is in the $1/\nu$ regime. On the other hand, if $\omega_E >> \omega_{\nabla B_a}$ and $\omega_E >> \nu_a(x)$, the particle is in the collisionless detrapping regime. Equation (6-18) is dominated by superbanana and superbanana plateau fluxes if $\omega_d^2 \simeq 0$. All of these regimes, as illustrated in Fig. 10 (page 38) in Chapter V, are, therefore, smoothly connected when using Eqs. (6-12) and (6-13).

CHAPTER VII

ATFSR PLASMA ANALYSIS WITH FIXED ELECTRIC FIELD PROFILE

The particle and energy transport equations defined in Chapter VI are solved for the ATFSR plasma to determine plasma heating requirements and to assess performance with and sensitivity to the radial electric field orientation and magnitude. The Plasma OPerating CONtours (POPCON) option of the 1-D WHIST transport code is used in these assessments.[36]

The WHIST code POPCON option allows scanning of large areas of plasma density-temperature space by providing feedback on the particle and energy sources. As shown in Fig. 11, the average electron density for each sweep is maintained constant by feedback on the pellet fueling, while the average temperature is linearly increased by feedback on the supplementary heating source. A set of data is generated along each scan that gives all particle and energy source and loss rates from the plasma along with major plasma parameters. These data are used to generate contour plots of radio-frequency heating power, fusion power output, neutron power to the first wall, etc., illustrating the plasma power balance properties defined in Chapter II.

The particle and energy sources and sinks from fusion account for the primary fuel reaction, D-T, as well as D-D and T-T. Separate deuterium and tritium pellets are used in ATFSR. A "continuous" pellet model is used yielding a continuous, rather than discrete, fuel source, eliminating minor fluctuations in the computations. Increasing the pellet size and velocity increases the penetration depth, producing higher power output due to profile peaking.

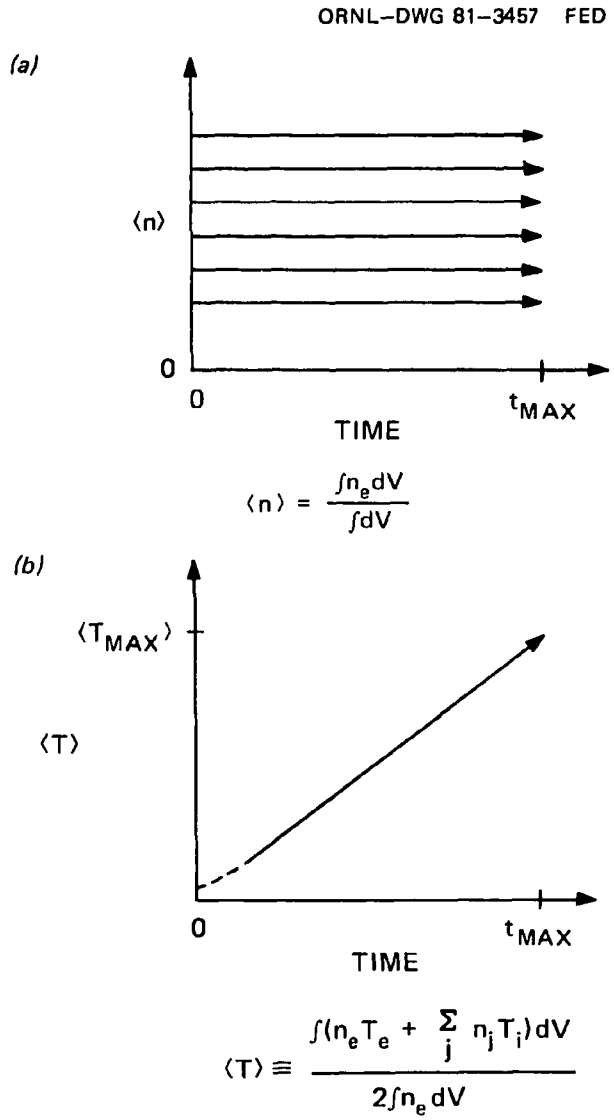

Fig. 11. WHIST code POPCON option method of scanning density-temperature space. To force a time-dependent transport code to scan a prescribed range of density-temperature space, (a) the average density $\langle n \rangle$ for each sweep is maintained constant by feedback on the relevant fueling source, while (b) the average temperature $\langle T \rangle$ is linearly increased by feedback on the supplementary heating source. The maximum average temperature attained is $\langle T_{max} \rangle$ and the total time of the linear ramp is t_{max}.

A Gaussian supplementary heating profile of the form

$$H(r) \sim \exp\left[-\left(2\,\frac{r}{\bar{a}}\right)^2\right] \tag{7-1}$$

is used to simulate radio-frequency heating. Either ion cyclotron range of frequency heating (ICRH) or electron cyclotron range of frequency heating (ECRH) is allowed by inputting energy to the ions, electrons, or both.

As introduced in Chapter VI, the reference transport model for the total particle flux is

$$\Gamma_a = \Gamma_a^{na} - (D_a^{ax} + d_a^{an})\frac{\partial n_a}{\partial \rho} \quad , \tag{7-2}$$

where D_a^{ax} is the neoclassical particle diffusion coefficient of an axisymmetric torus and d_a^{an} is an Alcator-like[37] particle diffusion coefficient given by

$$d_a^{an} = \frac{1.5 \times 10^{12}}{n_e} \quad (\mathrm{m^2/s}) \ . \tag{7-3}$$

The axisymmetric particle diffusion coefficient accounts for all particles not helically trapped. The anomalous coefficient simulates plasma edge turbulence.

The reference transport model for the total ion heat flux is

$$Q_i = Q_i^{na} - \chi_i^{ax}\left(\sum_j n_j\right)\frac{\partial T_i}{\partial \rho} \tag{7-4}$$

for all ion species "j," where χ_i^{ax} is the axisymmetric thermal ion conductivity. The total electron heat flux is

$$Q_e = Q_e^{na} - (\chi_e^{ax} + \chi_e^{an}) n_e \frac{\partial T_e}{\partial \rho} \ , \tag{7-5}$$

where χ_e^{ax} is the neoclassical axisymmetric thermal electron conductivity and χ_e^{an} is an Alcator-like thermal electron conductivity given by

$$\chi_e^{an} = \frac{4.5 \times 10^{12}}{n_e} \quad (\mathrm{m}^2/\mathrm{s}) \ . \tag{7-6}$$

In order to illustrate the importance of a radial electric field, $E_r = -\nabla\phi$, in stellarator/torsatron particle and energy transport, a parabolic potential profile of the form

$$\phi(r) = -\xi T_i(0) \left[\frac{r}{\bar{a}} \right]^2 \tag{7-7}$$

is input to the equations for nonambipolar particle and heat flux due to helical trapping. The parameter ξ is used to characterize the magnitude of the radial potential. As shown in Fig. 12 for ATF parameters, increasing values of $|\xi|$ significantly decrease χ as collision frequency is decreased, regardless of E_r orientation.

WHIST code POPCON plots for the ATFSR are made for $\xi = 1$–4. Positive radial electric field orientation, $\xi > 0$, indicates confinement governed by

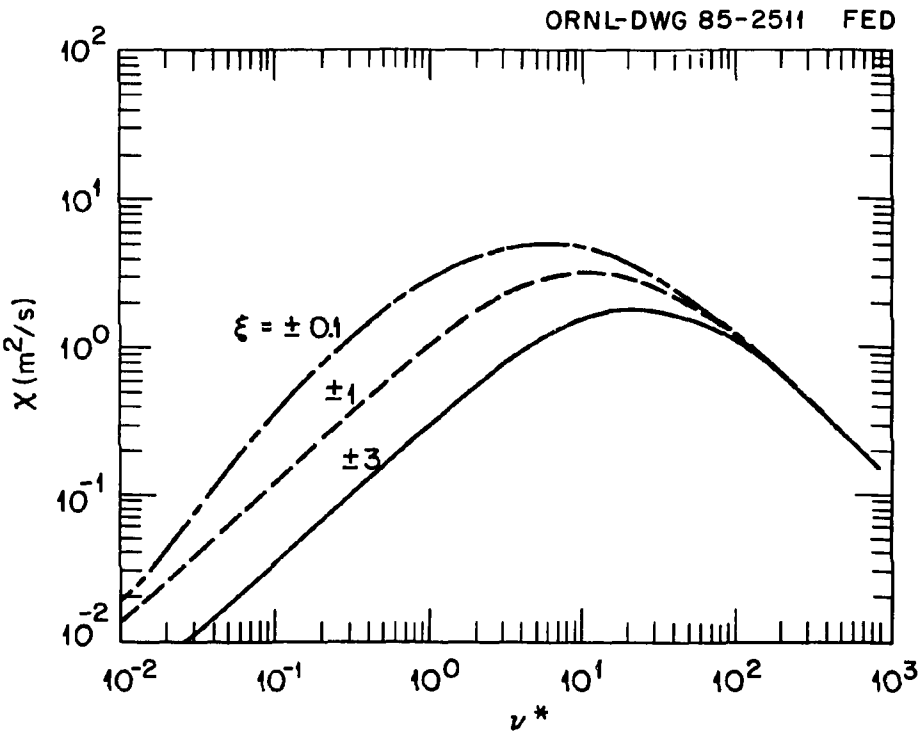

Fig. 12. Heat conductivity χ versus dimensionless collision frequency ν^* ($= \nu_e/\epsilon_t\omega_{hb}$) in the ATF for increasing values of $|\xi|$.

electron losses. ICRH is assumed for bulk plasma heating to ignition. This arbitrary combination of electric field orientation and ion heating is found in Chapter VIII to be optimal for approach to ignition. Supplementary heating power, fusion power, Q, and average toroidal beta contours are shown in Figs. 13 and 14 for ξ values of 2 and 4, respectively. For these plots, the reference transport model is used, exclusive of anomalous coefficients. Since energy confinement time scales inversely with ν_e and, therefore, density, for pure neoclassical processes, the ignition region that appears in the auxiliary power contours for the ξ value of 4 is independent of density.

Figure 15 illustrates the contours obtained for $\xi = 4$ when the complete reference transport model is used. Since the ambipolar anomalous coefficients are inversely proportional to density, only the low density areas of the plots are affected. The inclusion of the anomalous terms, depicting plasma edge turbulence, simulates experimental results more accurately than can be obtained from the neoclassical model alone.[38] An inspection of Fig. 15 indicates that a low density startup would require less than 20 MW of ICRH power deposited in the plasma in order to achieve ignition. In fact, less than 40 MW of deposited power appears to be satisfactory for a high density startup. However, the radial electric field may not always be directed radially outward, as is assumed in these figures. As will be shown in Chapter VIII, large areas of density-temperature space may be dominated by ion loss, requiring substantially more heating power to maintain a power balance.

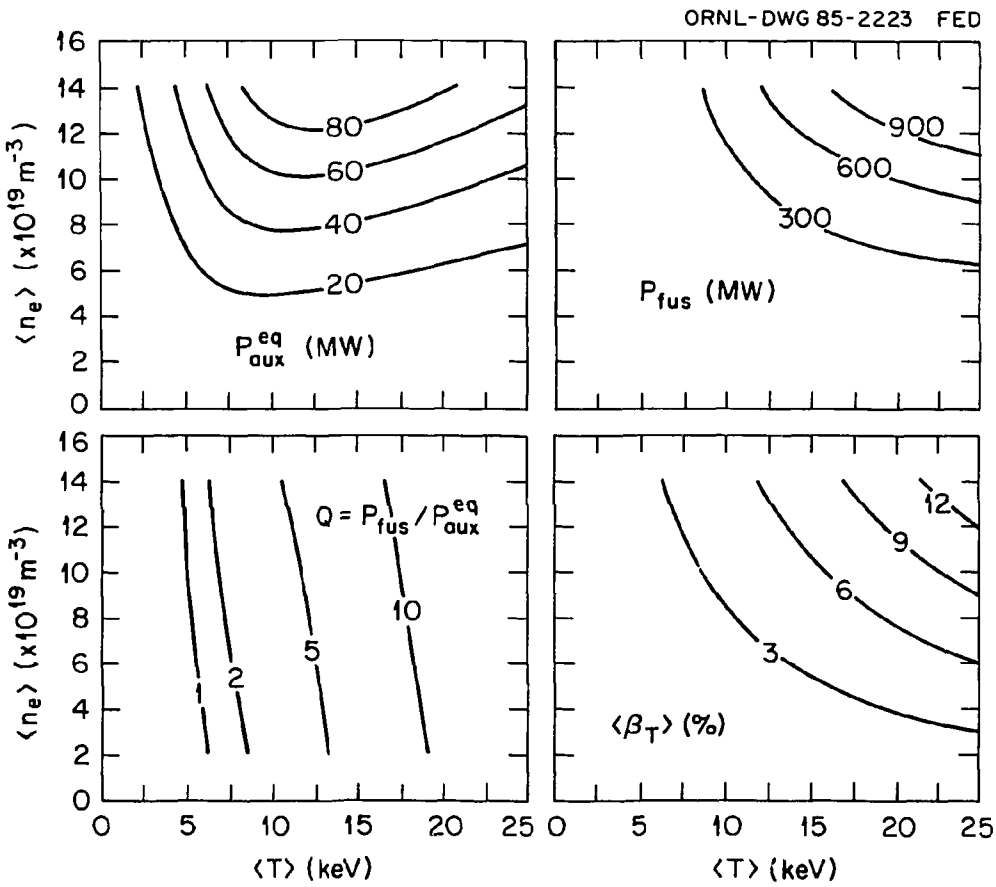

Fig. 13. ATFSR steady-state contours for neoclassical confinement with $\xi = 2$ and ICRH. The contours are supplementary heating (P_{aux}^{eq}), fusion power (P_{fus}), Q (P_{fus}/P_{aux}^{eq}), and toroidal beta ($\langle\beta_T\rangle$), shown for average electron density ($\langle n_e\rangle$) vs average temperature ($<T>$).

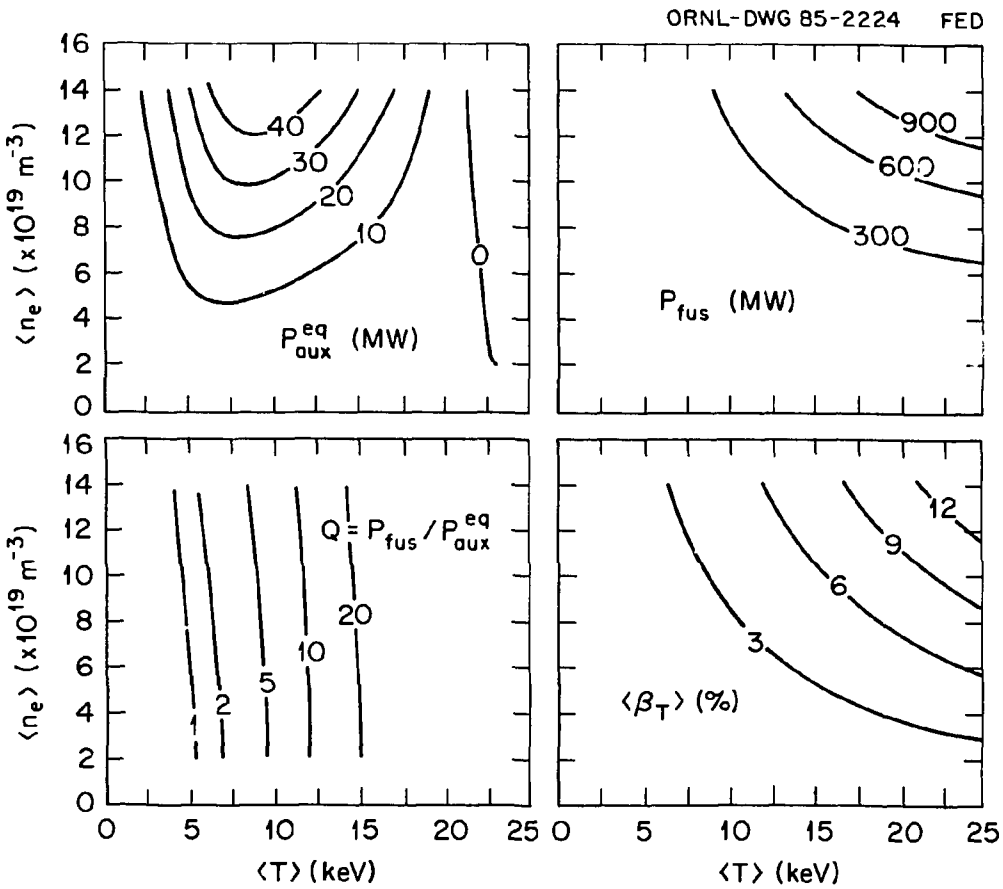

Fig. 14. ATFSR steady-state contours for neoclassical confinement with $\xi = 4$ and ICRH. The contours are supplementary heating (P_{aux}^{eq}), fusion power (P_{fus}), Q (P_{fus}/P_{aux}^{eq}), and toroidal beta ($\langle \beta_T \rangle$), shown for average electron density ($\langle n_e \rangle$) vs average temperature ($\langle T \rangle$).

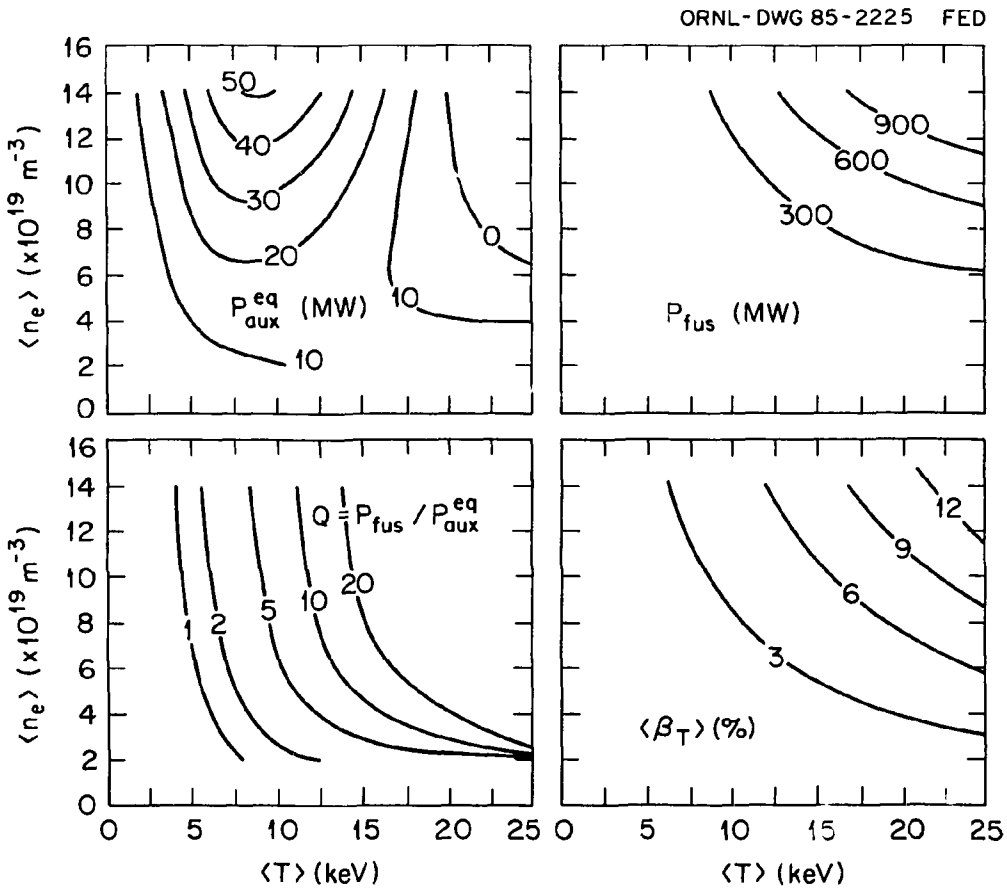

Fig. 15. ATFSR steady-state contours for neoclassical and anomalous confinement with $\xi = 4$ and ICRH. The contours are supplementary heating (P_{aux}^{eq}), fusion power (P_{fus}), Q (P_{fus}/P_{aux}^{eq}), and toroidal beta ($\langle \beta_T \rangle$), shown for average electron density ($\langle n_e \rangle$) vs average temperature ($\langle T \rangle$).

CHAPTER VIII

ATFSR PLASMA ANALYSIS WITH SELF-CONSISTENT ELECTRIC FIELD PROFILE

The transition from an intermediate collisionality regime in which transport coefficients scale as $1/\nu$ to the low-collisionality regime in which these coefficients are proportional to ν is of particular importance for reactor transport modeling and plasma performance assessment. The transition from ion-dominated losses to electron-dominated losses causes a reversal of the radial electric field, with the potential for significant enhancement of ion confinement.

The value of E_r may be determined self-consistently using the transport equations,[39] rather than setting the potential profile such that transport is always dominated by electron losses, as was done in Chapter VII. An algebraic and a differential formulation for the radial electric field are solved along with the particle and energy transport equations. The algebraic model calculates E_r from the steady-state ambipolarity constraint

$$\sum_a e_a \vec{\Gamma}_a \cdot \nabla\psi = 0 \ , \tag{8-1}$$

where $e_a = Z_a e$, whereas the differential model is radially nonlocal, employing a higher-order particle flux diffusion term.

From Maxwell's equation $\nabla \cdot \vec{E} = \rho\epsilon_0^{-1}$,

$$\frac{\partial}{\partial t}(\vec{E} \cdot \nabla\psi) = -\epsilon_0^{-1}(\vec{J} \cdot \nabla\psi) \ , \tag{8-2}$$

where ρ is charge density, ϵ_0 is the permittivity of free space, and ψ is magnetic flux. Two types of radial currents occur:

$$\text{conduction current} = \vec{\Gamma}_a \cdot \nabla\psi \ , \tag{8-3}$$

$$\text{polarization current} = \frac{n_a m_a}{e_a} \frac{c^2}{B^2} \left(\frac{\partial \vec{E}}{\partial t} \cdot \nabla\psi \right) \ , \tag{8-4}$$

where $\vec{\Gamma}_a \cdot \nabla\psi$ is the gradient-driven radial particle flux, n_a is the particle density, m_a is the particle mass, and c is the velocity of light. Inserting Eqs. (8-3) and (8-4) into Eq. (8-2) yields

$$\left(1 + \epsilon_0^{-1} \sum_a n_a m_a \frac{c^2}{B^2} \right) \frac{\partial \vec{E}}{\partial t} \cdot \nabla\psi = -\epsilon_0^{-1} \sum_a e_a \vec{\Gamma}_a \cdot \nabla\psi \ . \tag{8-5}$$

Substituting the Alfven speed V_A,

$$\frac{1}{V_A^2} = \epsilon_0^{-1} \sum_a \frac{n_a m_a}{B^2} \tag{8-6}$$

yields

$$\left(1 + \frac{c^2}{V_a^2} \right) \frac{\partial \vec{E}}{\partial t} \cdot \nabla\psi = -\epsilon_0^{-1} \sum_a e_a \vec{\Gamma}_a \cdot \nabla\psi \ . \tag{8-7}$$

Since $\vec{E}_r = -\nabla\phi$ and $\nabla\phi(\psi) = \frac{\partial\phi}{\partial\psi}\nabla\psi = \phi'\nabla\psi$,

$$\frac{\partial\phi'}{\partial t} = \frac{\epsilon_0^{-1}}{|\nabla\psi|^2\left[1 + \frac{c^2}{V_A^2}\right]} \sum_a e_a \vec{\Gamma}_a \cdot \nabla\psi \ . \tag{8-8}$$

The polarization current is small and can be ignored since $V_a \ll c$. For the steady-state algebraic model, $\partial\phi'/\partial t = 0$, yielding Eq. (8-1). In this model, the fluxes are driven by linear gradients of density, .emperature, and electrostatic potential, all considered to be constant on flux surface.

The differential model is, however, radially nonlocal. A higher order particle flux due to the finite size of the particle orbit is included. The higher order particle flux provides coupling between two adjacent flux surfaces, removing the problem of electric field discontinuity (opposite directions) that may exist with the algebraic model. With the higher order differential term included,[40] Eq. (8-8) becomes

$$\frac{\partial\phi'}{\partial t} = \frac{\epsilon_0^{-1}}{|\nabla\psi|^2\left[1 + \frac{c^2}{V_A^2}\right]} \sum_a e_a \vec{\Gamma}_a \cdot \nabla\psi$$

$$+ \ \frac{1}{V'} \frac{\partial}{\partial\psi}\left[V' D_E(\psi) \frac{\partial\phi'}{\partial\psi}\right] , \tag{8-9}$$

where $D_E(\psi)$ is the electric field diffusion coefficient. The boundary conditions applied to the differential formulation are

$$(1) \quad \phi'(\rho = 0) = 0 \ , \tag{8-10}$$

$$(2) \quad \Gamma_e(\rho = \bar{a}) = \Gamma_i(\rho = \bar{a}) \ . \tag{8-11}$$

Condition (1) is based upon symmetry considerations, and condition (2) indicates that at the plasma edge the ion flux is equal to the electron flux.

The steady-state ambipolarity constraint Eq. (8-1) has only one solution if both ions and electrons are in the $1/\nu$ regime or in the radial electric field collisionless detrapping regime. In the $1/\nu$ regime, ion loss predominates, forming a negative electric field that retards their flow. This solution is referred to as the ion root. In the collisionless detrapping regime, electron loss predominates, forming a positive electric field. This solution is the electron root. Various plasma species, however, are typically in different collisionality regimes such that the ambipolarity constraint has multiple solutions.

Figure 16 contains illustrations of the ion and electron fluxes' effective ripple particle diffusion coefficient

$$D_{\text{eff}}^{a,rp} = D_{n_a}^{rp} + q_a D_{\phi_a}^{rp} \frac{n_a}{T_a} \left(\frac{\partial \phi}{\partial \rho} \Big/ \frac{\partial n_a}{\partial \rho} \right) + D_{T_a}^{rp} \frac{n_a}{T_a} \left(\frac{\partial T_a}{\partial \rho} \Big/ \frac{\partial n_a}{\partial \rho} \right) \tag{8-12}$$

as a function of ϕ'/T_i', for volume-averaged electron densities of 4.0×10^{19} m^{-3} and 1.2×10^{20} m^{-3}. Plots are shown for ion temperatures of 5, 15,

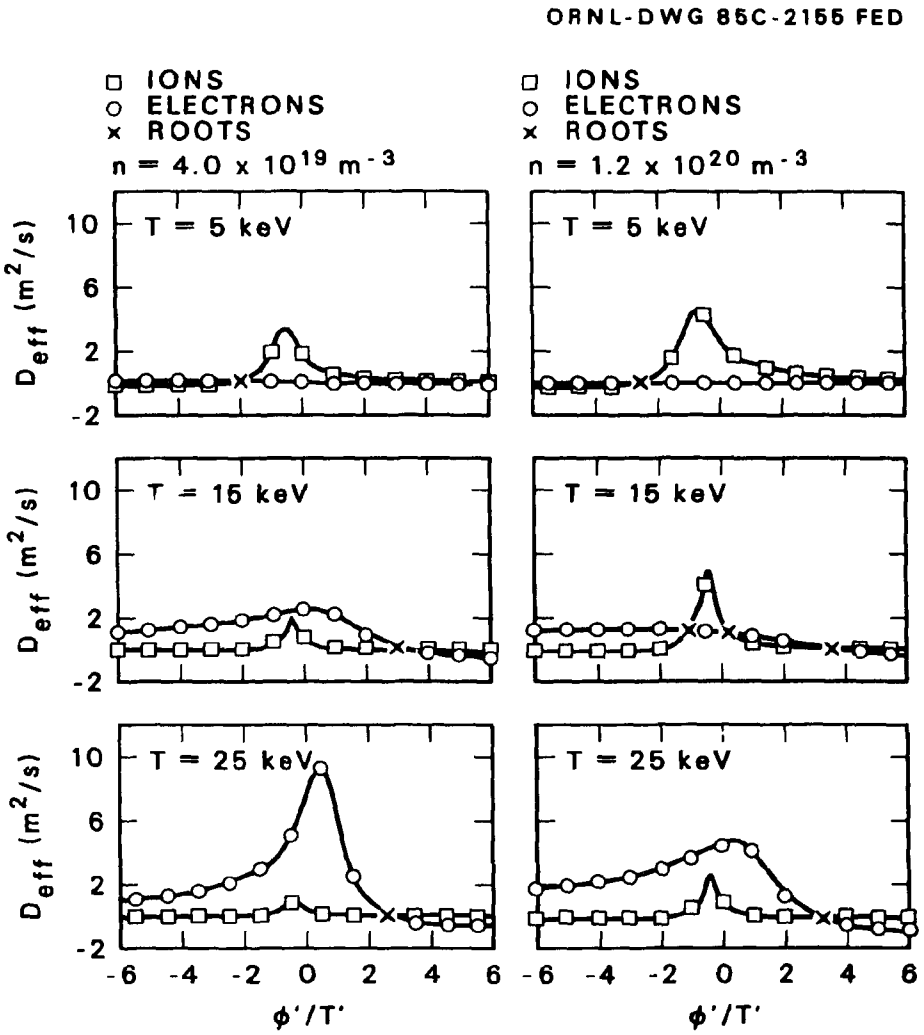

Fig. 16. ATFSR ambipolar particle fluxes versus ϕ'/T' for low and high densities with ion temperatures of 5, 15, and 25 keV. The low density is $n = 4.0 \times 10^{19}\,\mathrm{m}^{-3}$ and the high density is $n = 1.2 \times 10^{20}\,\mathrm{m}^{-3}$.

and 25 keV, with electron temperatures one-half of the ion values. The on-axis magnetic field strength is 5 T and the plots illustrate conditions at the half-radius, $r/\bar{a} = 0.5$. In the low density case, 4.0×10^{19} m^{-3}, the steady-state ambipolarity condition has only one solution at each of the temperatures. A negative electric field, or ion root, occurs for the 5-keV temperature, and a positive electric field, or electron root, for both higher temperatures. However, in the high density case, 1.2×10^{20} m^{-3}, a single ion root exists at low temperature and a single electron root at the high temperature, while the 15-keV temperature plot exhibits one ion root and two electron roots.

As illustrated, a lowering of the density encourages the transition to the electron root. Since electron collisionality drops with density, the electrons move further into the $1/\nu$ regime, with the electric field becoming positive to hold in the increased electron losses. For the case of three roots, it has been shown[41] through linearization and solution of Eq. (8-8) that the central node is always unstable. However, both an ion root and a lower-flux electron root satisfy the ambipolarity constraint at $\langle n_e \rangle = 1.2 \times 10^{20}$ m^{-3} and 15 keV. Therefore, simply setting the potential profile as positive or negative is insufficient, and either the algebraic or the differential electric field formulation must be solved, allowing for a root change. A root jump will cause a sudden change in the self-consistent flux. Since a single root cannot be considered to exist at all plasma radii, the algebraic model may lead to discontinuous jumps in the radial electric field. Therefore, the differential model is used in the transport analysis to provide continuous solutions, smoothly connecting the ion-loss–dominated regime to the electron-loss–dominated regime.

Illustrations of the ion and electron fluxes' effective ripple particle diffusion coefficient D_{eff} plotted as a function of ϕ'/T_i', such as those in Fig. 16, and illustrations of the ion and electron fluxes' effective ripple heat conductivity

$$\chi_{\text{eff}}^{a,rp} = \chi_{T_a}^{rp} + q_a \chi_{\phi_a}^{rp} \left(\frac{\partial \phi}{\partial \rho} \Big/ \frac{\partial T_a}{\partial \rho} \right) + \chi_{n_a}^{rp} \frac{T_a}{n_a} \left(\frac{\partial n_a}{\partial \rho} \Big/ \frac{\partial T_a}{\partial \rho} \right) \tag{8-13}$$

plotted as a function of temperature are used to determine the impact on transport of individually increasing the magnetic field, the average plasma radius, and the plasma aspect ratio. Figure 17 has plots of D_{eff} (at $T = 15$ keV) and χ_{eff} for the base reactor with $\bar{a} = 1.0$ m, $A = 7$, and $B_\phi = 5$ T and for a reactor where B_ϕ is increased to 7 T. Figure 18 has the same plots for an increase of $\bar{a}_p$ to 1.5 m and for an increase of the plasma aspect ratio to 10.

Figure 17 indicates that increased B_ϕ drives the solution toward the ion root. The transition from the ion to the electron root is most easily obtained at low B_ϕ. Ripple conductivity slightly decreases with increasing B_ϕ. Figure 18 indicates that increased average plasma radius also drives the solution toward the ion root. In fact, at $T = 15$ keV only the ion root exists. Therefore, the transition from the ion to the electron root is easiest for smaller plasma radii. Ripple conductivity slightly increases with increasing $\bar{a}_p$. Increasing the aspect ratio again drives the solution toward the ion root, with the transition from the ion to the electron root most easily obtained at lower plasma aspect ratios. Ripple conductivity slightly decreases with increasing A. Therefore, substantial increases in magnetic field strength, average plasma radius, and plasma aspect ratio only result in driving the solution toward the ion root. The selection in

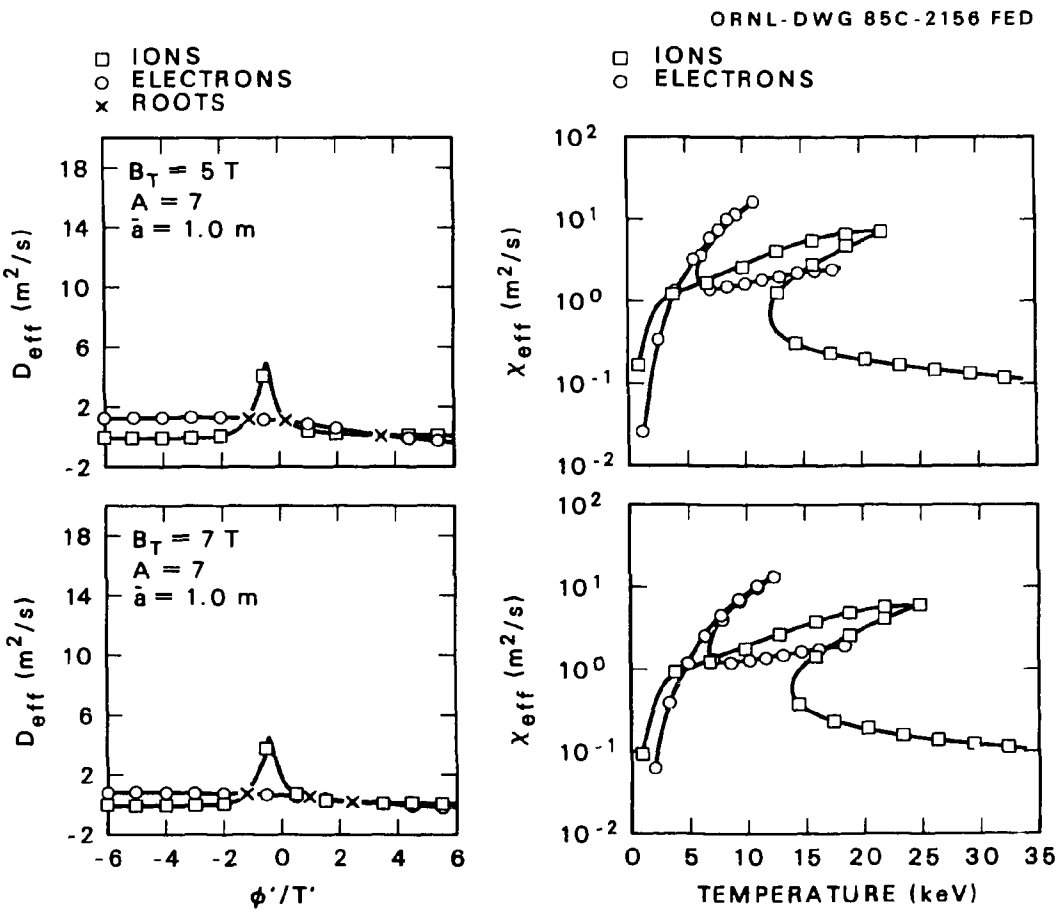

Fig. 17. ATFSR ambipolar particle fluxes versus ϕ'/T' and heat conductivities versus T for base case and for increased toroidal field. Base case is given by $B_T = 5$ T, $A = 7$, $\bar{a} = 1.0$ m, and increased toroidal field is given by $B_T = 7$ T, $A = 7$, $\bar{a} = 1.0$ m.

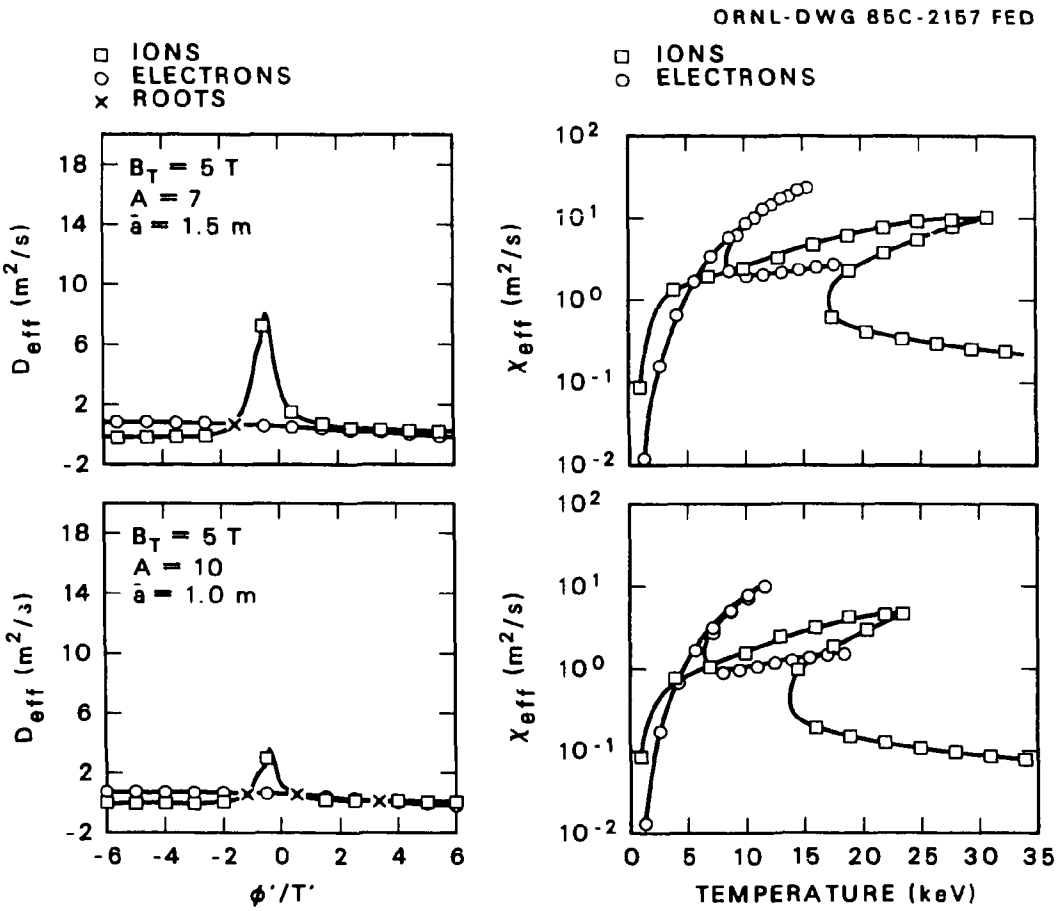

Fig. 18. ATFSR ambipolar particle fluxes versus ϕ'/T' and heat conductivities versus T for increased plasma radius and for increased aspect ratio. Increased plasma radius is given by $B_T = 5$ T, $A = 7$, $\bar{a} = 1.5$ m, and increased aspect ratio is given by $B_T = 5$ T, $A = 10$, $\bar{a} = 1.0$ m.

Chapters II through IV of a small average plasma radius of 1 m, a plasma aspect ratio of 7, and a moderate on-axis magnetic field strength of 5 T enhances transition to the desired electron root and yields conduction coefficients equivalent or superior to considerably larger machines with the same magnetic field, even though the particle and energy confinement times increase as $(\bar{a})^2$.

Using the differential model for Eq. (8-9) for the self-consistent determination of the radial electric field profile, WHIST code POPCON plots for the ATFSR are shown in Figs. 19 and 20 for ICRH and ECRH, respectively. The reference transport model is used, exclusive of anomalous coefficients. Comparing Fig. 19 with Fig. 14 (page 54), over 300 MW of ICRH power deposited in the plasma is necessary for a high density startup, substantially more than the 40 MW required when a positive radial electric field is assumed for all operating space conditions. At low temperatures, both ions and electrons are in the $1/\nu$ regime, and since the electron collisionality is larger than the ion collisionality, the ion losses are larger than the electron losses. The radial electric field is negative, retarding the ion flow. As power is given to the ions during startup, the ν regime is eventually entered. The electrons, heated by rethermalization with the ions, remain in the $1/\nu$ regime, eventually following the ions into the ν regime as the average plasma temperature increases. Since both species are now in the collisionless detrapping regime with the electron collisionality greater than the ion collisionality, the radial electric field has reversed and become positive, holding in the electron flow. The ion regime ($\phi < 0$), the transition regime ($\phi \sim 0$), and the electron regime ($\phi > 0$) are shown in Figs. 19 and 20.

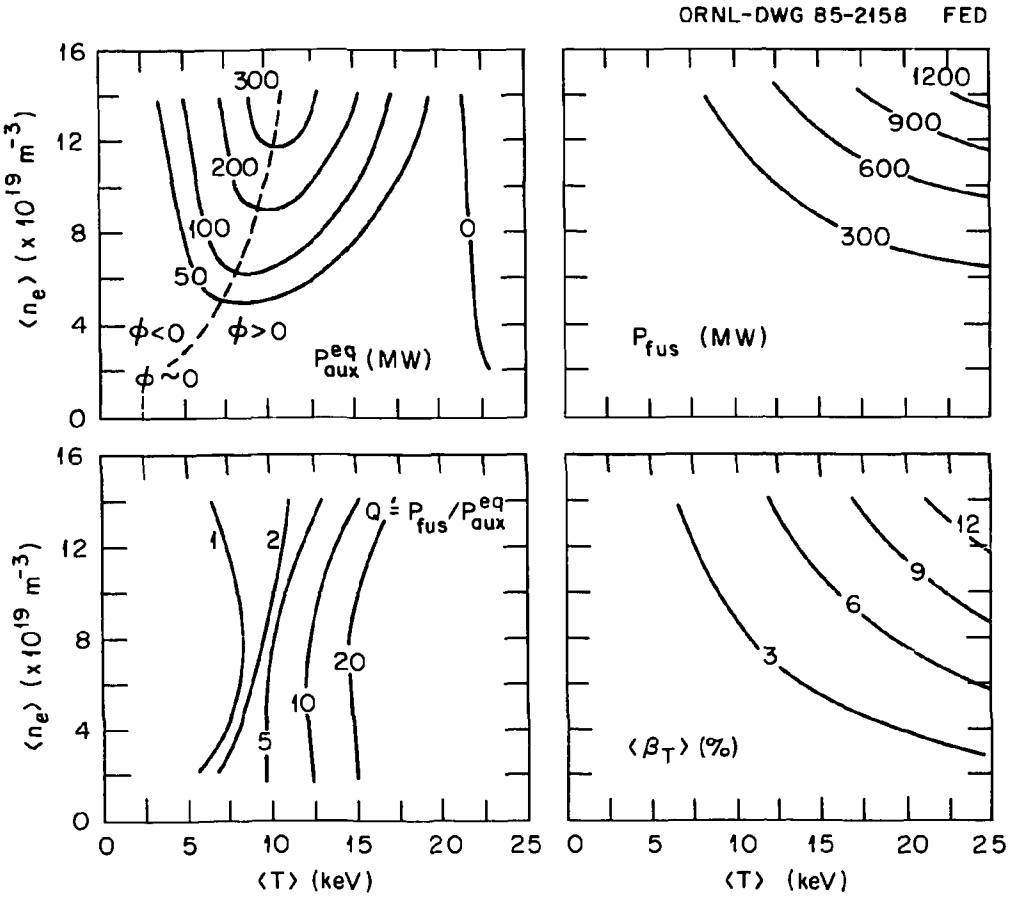

Fig. 19. ATFSR steady-state contours for neoclassical confinement and ICRH, with self-consistent E_r evolution through the transition, $\xi = 4$ thereafter. The contours are supplementary heating (P^{eq}_{aux}), fusion power (P_{fus}), $Q(P_{fus}/P^{eq}_{aux})$, and toroidal beta ($\langle \beta_T \rangle$), shown for average electron density ($\langle n_e \rangle$) vs average temperature ($<T>$).

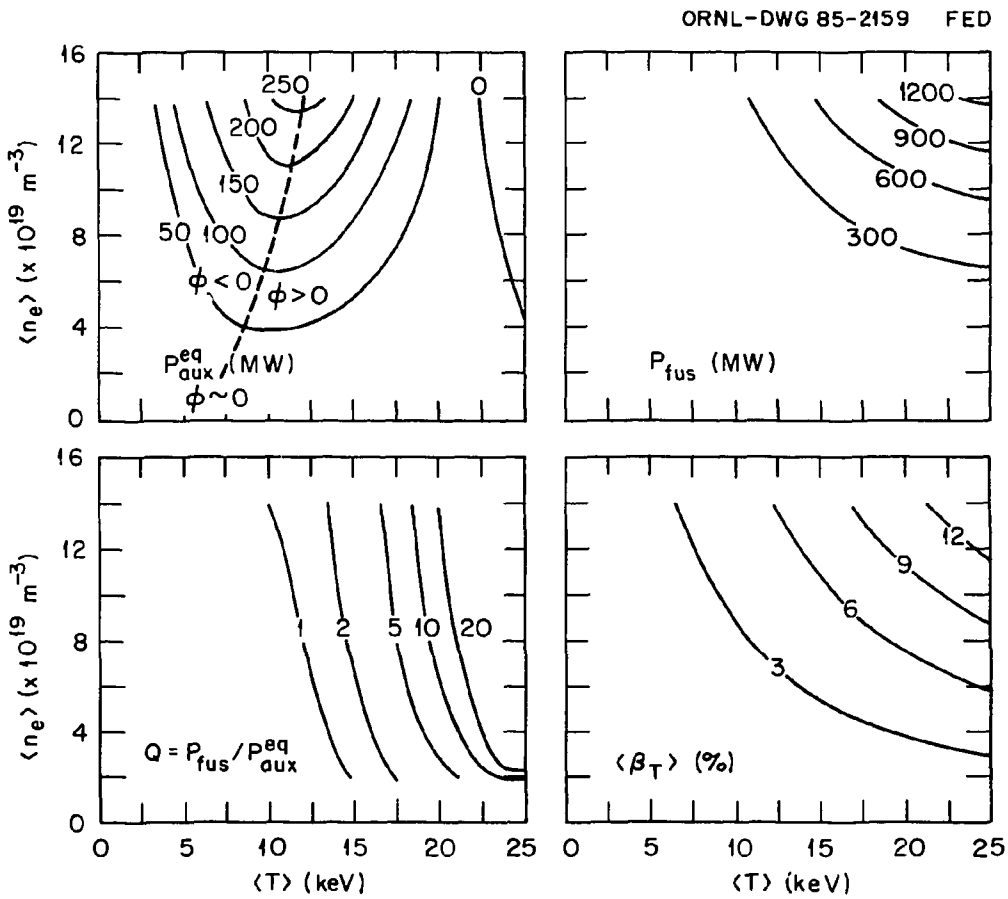

Fig. 20. ATFSR steady-state contours for neoclassical confinement and ECRH, with self-consistent E_r evolution through the transition, $\xi = 4$ thereafter. The contours are supplementary heating (P^{eq}_{aux}), fusion power (P_{fus}), $Q(P_{fus}/P^{eq}_{aux})$, and toroidal beta ($\langle\beta_T\rangle$), shown for average electron density ($\langle n_e\rangle$) vs average temperature ($<T>$).

When ECRH is employed, somewhat less high density startup power is required, since the electrons will be in the $1/\nu$ regime at lower collisionality than in the ICRH case, with electron losses exceeding ion losses sooner. However, regardless of the heating mechanism employed, a high density startup of the ATFSR does not appear to be feasible due to the excessive power requirements. The transition regime ($\phi \sim 0$) is best penetrated at low density and temperature. After the transition to the electron root is made, the density can be increased as the temperature increases.

Due to reduced alpha heating power available when using ECRH, the supplementary heating power contours of Fig. 20 are broader than those of Fig. 19, where ICRH is used. When this effect is coupled with that of the full reference transport model, including anomalous terms, Figs. 21 and 22 result. Since the ambipolar anomalous coefficients are inversely proportional to density, only the low density areas of the plots are changed. Although a low power startup path to ignition remains in Fig. 21 for ICRH, the power deposited in the plasma must exceed a minimum of 75 MW when ECRH is used in Fig. 22. Therefore, ICRH is the optimal heating mechanism when ignited operation is the objective. The optimal path in density-temperature space to reach the ATFSR's ignited operating point is discussed in Chapter IX.

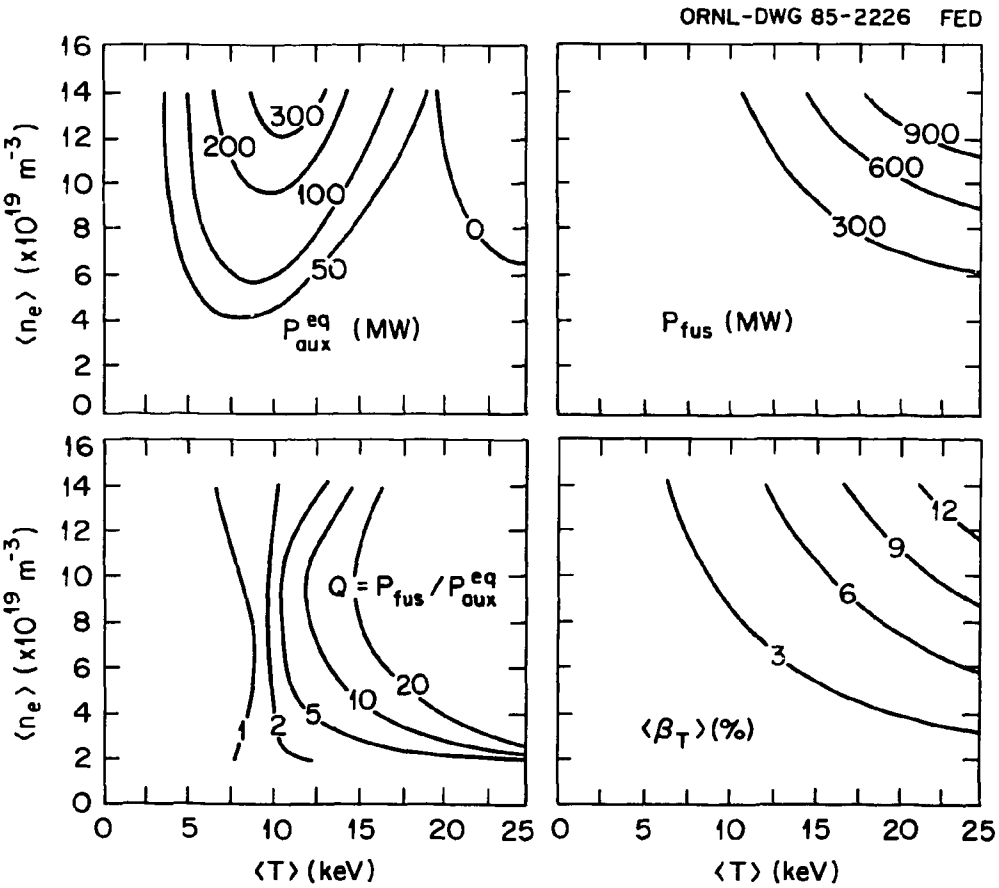

Fig. 21. ATFSR steady-state contours for neoclassical and anomalous confinement and ICRH, with self-consistent E_r evolution through the transition, $\xi = 4$ thereafter. The contours are supplementary heating (P_{aux}^{eq}), fusion power (P_{fus}), $Q(P_{fus}/P_{aux}^{eq})$, and toroidal beta ($\langle\beta_T\rangle$), shown for average electron density ($\langle n_e\rangle$) vs average temperature ($<T>$).

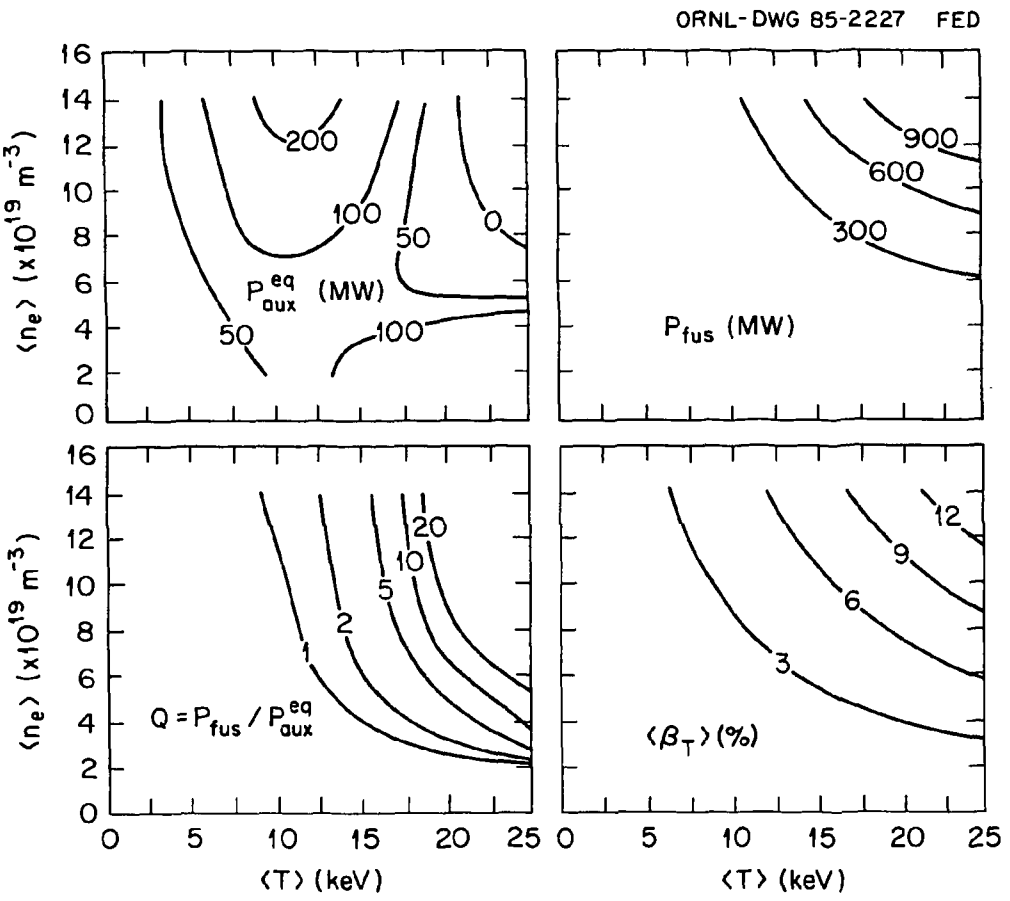

Fig. 22. ATFSR steady-state contours for neoclassical and anomalous confinement and ECRH, with self-consistent E_r evolution through the transition, $\xi = 4$ thereafter. The contours are supplementary heating (P^{eq}_{aux}), fusion power (P_{fus}), $Q(P_{fus}/P^{eq}_{aux})$, and toroidal beta ($\langle\beta_T\rangle$), shown for average electron density ($\langle n_e\rangle$) vs average temperature ($<T>$).

CHAPTER IX

ATFSR IGNITED PLASMA PARAMETERS AND POWER OUTPUTS

To initiate startup, an equal part D-T gas mixture sufficient for an approximate total ion density of 2.0×10^{19} m^{-3} is introduced into the vacuum chamber. ICRH is used to break down the gas and heat the resulting plasma. Maintaining this low density, the plasma transitions onto the electron root at an average plasma temperature of 6 keV with only 15 MW of ICRH power deposited in the plasma. Assuming a 75% efficiency for ICRH coupling with the ions,[42] a total ICRH source of 20 MW is required to heat the ATFSR to ignition.

After the transition onto the electron root, feedback regulation of the fuel pellet injection and the radio-frequency power results in a gradual increase in the density and temperature. During this slow ramp-up to ignition, the fusion power output also increases gradually, preventing thermal shock of the blanket and shield materials. After ignition, the reactor is slowly brought to the full power operating point, the D-T density being increased to the steady-state value of 1.2×10^{20} m^{-3}. As shown in Fig. 23, which illustrates superimposed supplementary heating power, fusion power, and toroidal beta contours with the startup path, this operating point corresponds to an average plasma temperature of 20 keV and an average toroidal beta of ~9%. Table IV contains a summary of plasma parameters.

At low temperatures, radio-frequency heating balances the diffusion, conduction, and radiation power losses, as explained in Chapter II. Ignition occurs

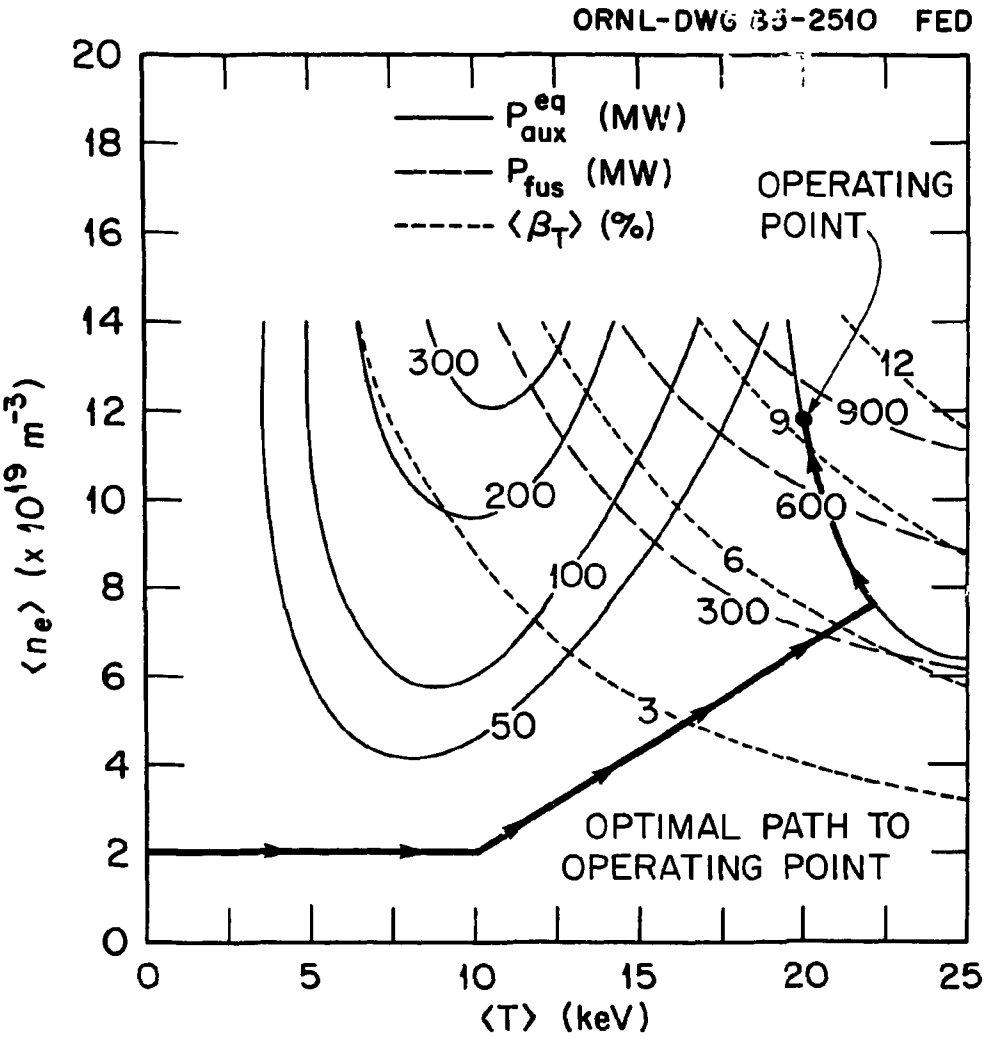

Fig. 23. ATFSR steady-state contours for neoclassical and anomalous confinement and ICRH, with self-consistent E_r evolution through the transition, $\xi = 4$ thereafter, with optimal heating path for startup and the final operating point. The contours are supplementary heating (P_{aux}^{eq}), fusion power (P_{fus}), and toroidal beta ($\langle\beta_T\rangle$), shown for average electron density ($\langle n_e \rangle$) vs average temperature ($\langle T \rangle$).

Table IV. ATFSR Plasma Parameters

Plasma major radius, R	7.0 m
Plasma average radius, $\bar{a}$	1.0 m
Plasma semiminor radius, a_p	0.78 m
Plasma semimajor radius, b_p	1.29 m
Plasma elongation	1.65
Plasma volume, V_p	138.2 m^3
Plasma aspect ratio, A	7.0
Average ion temperature, $<T_i>$	24 keV
Average electron temperature, $<T_e>$	18 keV
Reaction type	D-T
Average ion density, $<n_i>$	1.2×10^{20} m^{-3}
Average electron density, $<n_e>$	1.2×10^{20} m^{-3}
Average beta, $<\beta>$	0.09
Plasma heating technique	ICRF
Maximum heating power required	20 MW
Plasma fueling technique	pellet
Average ion energy confinement time, $<\tau_{E_i}>$	5 s
Average electron energy confinement time, $<\tau_{E_e}>$	0.5 s

when the energy input from fusion alphas, increasingly available to aid in heating the plasma during the density-temperature ramp-up, is alone great enough to overcome these power losses. The ignition curve represents an unstable temperature equilibrium. Once past ignition, the plasma continues to heat, perhaps to a second equilibrium where increased power losses due to synchrotron radiation and enhanced diffusion and conduction losses due to the approach of a beta limit might provide thermal stability. Therefore, to remain on the unstable ignited operating point, the ATFSR must employ a feedback control such as impurity addition and its subsequent radiative power emission.

The effects of impurities are not included in the transport analysis. However, if fuel ions, impurity ions, and electrons are all in the $1/\nu$ regime, the radial electric field would be negative in the direction to retard the loss of fuel ions and impurity ions. But if all of the species are in the collisionless detrapping regime, the radial electric field would be positive in the direction to retard the loss of electrons, and the impurity flux tends to be expelled.[43] Since this is the regime in which a torsatron reactor would operate, impurity confinement would be minimized.

The fusion power output at the operating point is 800 MW. When a typical blanket multiplication factor of 0.2 is considered, the total thermal power output is 928 MW. With the toroidal volume approximation $2\pi^2(\bar{a})^2R$, the fusion power density is 5.8 MW/m^3, and the thermal power density is 6.7 MW/m^3. Using the toroidal surface area approximation $4\pi^2\bar{a}R$, the first-wall neutron loading is 2.3 MW/m^2. Assuming a recirculating power fraction of 0.05 and a typical thermal conversion efficiency of 35%, based upon previous detailed thermal-hydraulic analyses of blanket and steam-supply systems,[44] the

net plant efficiency is ~33%. Therefore, the ATFSR produces a net electric power of 306 MWe when at the full power operation point. Table V contains a summary of all power output parameters.

In comparison with the previous stellarator/torsatron power reactor designs shown in Table I (page 2), the most obvious difference is the small physical size of the ATFSR itself: 1.0 m average plasma radius, 7.0 m major radius, with a plasma volume of 138.2 m^3. ATFSR values of the axial magnetic field, 5 T, maximum magnetic field at the coil, 10 T, and neutron wall loading, 2.3 MW/m^2, are all within near-term technology constraints, as opposed to several designs with excessive peak fields at the coil or wall loadings.

Note that $\langle\beta\rangle$ = 9% in the burn phase of ATFSR is considerably higher than most designs in Table I (page 2). But as described in Chapter III, the ATF-style magnetic configuration is able to achieve high stable beta values upon entering a second stability region, as illustrated in Fig. 5 (page 21). Since fusion and thermal power scale as the square of beta, the ATFSR configuration is capable of relatively high fusion and thermal power densities.

Table V. ATFSR Power Outputs

Fusion power, P_f	800 MW
Blanket neutron multiplication, m_b	0.2
Total thermal power, P_{th}	928 MW
Plasma fusion power density, FPD	5.8 MW/m^3
Plasma thermal power density, TPD	6.7 MW/m^3
First wall neutron loading, P_w	2.3 MW/m^2
Recirculating power fraction, ϵ	0.05
Thermal conversion efficiency, η	0.35
Net plant efficiency	0.33
Net electric power, P_e	306 MWe

CHAPTER X

CONCLUSIONS

A small, steady-state D-T torsatron power reactor based upon the ATF magnetic configuration is shown to be dependent on the presence of a moderate-to-strong radial electric field. Values of $e\phi/T > 3$ are necessary to achieve ignition, although Q values greater than ten may be attained if $e\phi/T \simeq 2$.

Existing neoclassical solutions for E_r show large resonant losses in the transition from the ion regime (high ν, $\phi < 0$) to the electron regime (low ν, $\phi > 0$). Since plasma initiation is in the ion regime while reactor operation will generally be in the electron regime, an efficient means for forcing the transition with low supplementary heating power is necessary. Decreases in average plasma radius, plasma aspect ratio, or magnetic field strength promote this transition. The ATFSR design, therefore, encourages plasma operation in the electron regime. At high densities an excessive amount of radio-frequency heating power is required to force the transition in the ATFSR, while at low density, less than 15 MW of absorbed ICRH power is necessary. When ECRH is employed, a more rapid transition into the electron regime is found. However, heating of the electrons is less efficient in reaching ignition (poor electron energy confinement and rethermalization with ions) with 75 MW of absorbed ECRH power required for ignition.

Anomalous transport was assumed to give no contribution to the radial electric field in this study. Theoretical models for the impact of a nonambipolar anomalous flow on the radial electric field remain to be developed. Ultimately,

the radial electric field and its effects on transport will have to be experimentally determined in devices such as the ATF in order to accurately project torsatron/stellarator fusion reactor potential.

The reactor engineering features of the ATFSR are all compatible with near-term technology constraints, with moderate neutron wall loading, maximum magnetic field at the helical coils, etc. The only possible exception may be insufficient shielding directly beneath the helical coils, requiring a somewhat smaller coil aspect ratio than employed for the ATF.

REFERENCES

1. R. L. Miller et al., Nucl. Technol./Fusion **4**, 1308 (1983).

2. B. Badger et al., *UWTOR-M: A Conceptual Modular Stellarator Reactor*, UWFOM-550, University of Wisconsin, Madison (1982).

3. J. Sheffield and R. Dory, "Cost Assessment of a Generic Magnetic Fusion Reactor," in *Proceedings of the 19th Annual Intersociety Energy Conversion Engineering*, San Francisco, California, August 1984.

4. J. F. Lyon et al., *Stellarator Physics Evaluation Studies*, ORNL/TM-8496, Oak Ridge Natl. Lab. (1983).

5. W. A. Houlberg and R. W. Conn, Nucl. Sci. Eng. **64**, 141 (1977).

6. T. J. Dolan, *Fusion Research*, Pergamon, New York (1982) 68.

7. T. J. Dolan, *Fusion Research*, Pergamon, New York (1982) 33.

8. W. M. Stacey, *Fusion Plasma Analysis*, Wiley, New York (1981) 286.

9. B. A. Carreras et al., *Equilibrium and Stability Properties of High Beta Torsatrons*, ORNL/TM-8752, Oak Ridge Natl. Lab. (1983) 3.

10. K. Miyamoto, *Plasma Physics for Nuclear Fusion*, MIT Press, Cambridge (1980) 207.

11. K. Miyamoto, Nucl. Fusion **18**, 243 (1978).

12. J. L. Shohet, *Fusion: Magnetic Confinement*, ed. E. Teller, Academic, New York (1981) 270.

13. K. Miyamoto, *Plasma Physics for Nuclear Fusion*, MIT Press, Cambridge (1980) 37.

14. K. Miyamoto, *Plasma Physics for Nuclear Fusion*, MIT Press, Cambridge (1980) 39.

15. B. A. Carreras et al., *Equilibrium and Stability Properties of High Beta Torsatrons*, ORNL/TM-8752, Oak Ridge Natl. Lab. (1983).

16. J. F. Lyon et al., *Stellarator Physics Evaluation Studies*, ORNL/TM-8496, Oak Ridge Natl. Lab. (1983).

17. [illegible] *to the Physics and Technol-*
[illegible] New York (1984) 111.

18. W. M. Stacey et al., *Tokamak Experimental Power Reactor Studies*, ANL/CTR-75-2, Argonne National Laboratory (1975) IV-18.

19. C. C. Baker et al., *STARFIRE: A Commercial Fusion Tokamak Power Plant Study*, ANL/FPP-80-1, Argonne National Laboratory (1980) 11-1.

20. F. F. Chen, *Introduction to Plasma Physics*, Plenum, New York (1974) 29.

21. J. L. Shohet, *Fusion: Magnetic Confinement*, ed. E. Teller, Academic, New York (1981) 262.

22. W. M. Stacey, *Fusion Plasma Analysis*, Wiley, New York (1981) 54.

23. R. A. Gross, *Fusion Energy*, Wiley, New York (1984) 116.

24. F. L. Hinton and R. D. Hazeltine, Rev. Modern Phys. **48**, 239 (1976).

25. A. Gibson and D. W. Mason, Plasma Phys. **11**, 121 (1969).

26. A. A. Galeev and R. Z. Sagdeev, *Advanced Plasma Physics* **6**, ed. A. Simon, Wiley, New York (1976) 311.

27. B. B. Kadomtsev and O. P. Pogutse, Nucl. Fusion **11**, 67 (1971).

28. K. C. Shaing and J. D. Callen, Phys. Fluids **26**, 3315 (1983).

29. R. H. Fowler et al., Phys. Fluids **28**, 338 (1985).

30. K. Miyamotó, *Plasma Physics for Nuclear Fusion*, MIT Press, Cambridge (1980) 213.

31. W. A. Houlberg and R. W. Conn, Nucl. Sci. Eng. **64**, 141 (1977).

32. W. A. Houlberg et al., *Computational Methods in Tokamak Transport*, ORNL/TM-8193, Oak Ridge Natl. Lab. (1982) 2.

33. L. Lapidus and G. F. Pinder, *Numerical Solution of Partial Differential Equations in Science and Engineering*, Wiley, New York (1982).

34. K. C. Shaing, Phys. Fluids **27**, 1567 (1984).

35. J. W. Connor and R. J. Hastie, Nucl. Fusion **13**, 221 (1973).

36. W. A. Houlberg et al., Nucl. Fusion **7**, 935 (1982).

37. T. J. Dolan, *Fusion Research*, Pergamon, New York (1982) 387.

38. H. Zushi et al., Nucl. Fusion **24**, 305 (1984).

39. D. E. Hastings et al., "The Ambipolar Electric Field in Stellarators," to be published in Phys. Fluids.

40. D. E. Hastings, Phys. Fluids **28**, 334 (1985).

41. K. C. Shaing, Phys. Fluids **27** 1567 (1984).

42. R. A. Gross, *Fusion Energy*, Wiley, New York (1984) 146.

43. K. C. Shaing, Phys. Fluids **26**, 3164 (1983).

44. C. C. Baker et al., *STARFIRE: A Commercial Fusion Tokamak Power Plant Study*, ANL/FPP-80-1, Argonne National Laboratory (1980) 13-1.

BIBLIOGRAPHY

1. Badger, B., et al., *UWTOR-M: A Conceptual Modular Stellarator Reactor*, UWFDM-550, University of Wisconsin, Madison (1982).

2. Baker, C. C., et al., *STARFIRE: A Commercial Fusion Tokamak Power Plant Study*, ANL/FPP-80-1, Argonne National Laboratory (1980).

3. Carreras, B. A., et al., *Equilibrium and Stability Properties of High Beta Torsatrons*, ORNL/TM-8752, Oak Ridge National Laboratory (1983).

4. Chen, F. F., *Introduction to Plasma Physics*, Plasma, New York (1974).

5. Connor, J. W., and R. J. Haste, Nucl. Fusion **13** (1973) 221.

6. Dolan, T. J., *Fusion Research*, Pergamon, New York (1982).

7. Fowler, R. H., et al., Phys. Fluids **28** (1985) 338.

8. Galeev, A. A., and R. F. Sagdeev, *Advanced Plasma Physics,* **6**, ed. A. Simon, Wiley, New York (1976).

9. Gibson, A., and D. W. Mason, Plasma Phys. **11** (1969) 121.

10. Gross, R. A., *Fusion Energy*, Wiley, New York (1984).

11. Hastings, D. E., Phys. Fluids **28** (1985) 334.

12. Hastings, D. E., et al., "The Ambipolar Electric Field in Stellarators," to be published in Phys. Fluids.

13. Hinton, F. L., and R. D. Hazeltine, Rev. Modern Phys. **48** (1976) 239.

14. Houlberg, W. A., and R. W. Conn, Nucl. Sci. Eng. **64** (1977) 141.

15. Houlberg, W. A., et al., Nucl. Fusion **7** (1982) 935.

16. Houlberg, W. A., et al., *Computational Methods in Tokamak Transport*, ORNL/TM-8193, Oak Ridge National Laboratory (1982).

17. Kadomtsev, B. B., and O. P. Pogutse, Nucl. Fusion **11** (1971) 67.

18. Lapidus, L., and G. F. Pinder, *Numerical Solution of Partial Differential Equations in Science and Engineering*, Wiley, New York (1982).

19. Lyon, J. F., et al., *Stellarator Physics Evaluation Studies*, ORNL/TM-8496, Oak Ridge National Laboratory (1983).

20. Miller, R. L., et al., Nucl. Technol./Fusion **4** (1983) 1308.

21. Miyamoto, K., Nucl. Fusion **18** (1978) 243.

22. Miyamoto, K., *Plasma Physics for Nuclear Fusion*, MIT Press, Cambridge (1980)

23. Shaing, K. C., and J. D. C Phys. Fluids **26** (1983) 3315.

24. Shaing, K. C., Phys. Fluids **26** (1983) 3164.

25. Shaing, K. C., Phys. Fluids **27** (1984) 1567.

26. Sheffield, J., and D ory, "Cost Assessment of A Generic Magnetic Fusion Reactor," *19th Annual Intersociety Energy Conversion Engineering*, San Francisco, August 1984.

27. Shohet, J. L., *Fusion: Magnetic Confinement*, ed. E. Teller, Academic, New York (1981).

28. Stacey, W. M., *Fusion Plasma Analysis*, Wiley, New York (1981).

29. Stacey, W. M., *Fusion: An Introduction to the Physics and Technology of Magnetic Confinement Fusion*, Wiley, New York (1984).

30. Stacey, W. M., et al., *Tokamak Experimental Power Reactor Studies*, ANL/CTR-75-2, Argonne National Laboratory (1975).

31. Zushi, H., et al., Nucl. Fusion **24** (1984) 305.

ORNL/TM-9533
Dist. Category UC-20

INTERNAL DISTRIBUTION

1. L. A. Berry
2. B. A. Carreras
3. R. A. Dory
4. J. Dunlap
5. J. H. Harris
6. H. H. Haselton
7. P. N. Haubenreich
8. C. L. Hedrick
9–10. W. A. Houlberg
11. M. S. Lubell
12. J. F. Lyon
13. Y-K. M. Peng
14. J. A. Rome
15. M. J. Saltmarsh
16. T. E. Shannon
17. D. J. Sigmar
18–19. N. A. Uckan
20–21. Laboratory Records Department
22. Laboratory Records, ORNL-RC
23. Document Reference Section
24. Central Research Library
25. Fusion Energy Division Library
26. Fusion Energy Division Publications Office
27. ORNL Patent Office

EXTERNAL DISTRIBUTION

28–29. J. T. Lacatski, 330 Emory Drive, Daytona Beach, FL 32018
30. Office of the Assistant Manager for Energy Research and Development, Department of Energy, Oak Ridge Operations, Box E, Oak Ridge, TN 37831
31. J. D. Callen, Department of Nuclear Engineering, University of Wisconsin, Madison, WI 53706
32. R. W. Conn, Department of Chemical, Nuclear, and Thermal Engineering, University of California, Los Angeles, CA 90024
33. S. O. Dean, Director, Fusion Energy Development, Science Applications, Inc., 2 Professional Drive, Gaithersburg, MD 20760
34. H. K. Forsen, Bechtel Group, Inc., Research Engineering, P.O. Box 3965, San Francisco, CA 94105
35. J. R. Gilleland, GA Technologies, Inc., Fusion and Advanced Technology, P.O. Box 85608, San Diego, CA 92138
36. R. W. Gould, Department of Applied Physics, California Institute of Technology, Pasadena, CA 91125
37. R. A. Gross, Plasma Research Laboratory, Columbia University, New York, NY 10027
38. D. M. Meade, Princeton Plasma Physics Laboratory, P.O. Box 451, Princeton, NJ 08544

39. P. J. Reardon, Princeton Plasma Physics Laboratory, P.O. Box 451, Princeton, NJ 08544
40. W. M. Stacey, Jr., School of Mechanical Engineering, Georgia Institute of Technology, Atlanta, GA 30332
41. D. Steiner, Nuclear Engineering Department, NES Building, Tibbetts Avenue, Rensselaer Polytechnic Institute, Troy, NY 12181
42. R. Varma, Physical Research Laboratory, Navrangpura, Ahmedabad 380009, India
43. Bibliothek, Max-Planck Institut fur Plasmaphysik, D-8046 Garching, Federal Republic of Germany
44. Bibliothek, Institut fur Plasmaphysik, KFA, Postfach 1913, D-5170 Julich, Federal Republic of Germany
45. Bibliotheque, Centre de Recherches en Physique des Plasmas, 21 Avenue des Bains, 1007 Lausanne, Switzerland
46. Bibliotheque, Service du Confinement des Plasmas, CEA, B.P. 6, 92 Fontenay-aux-Roses (Seine), France
47. Documentation S.I.G.N., Departement de la Physique du Plasma et de la Fusion Controlee, Centre d'Etudes Nucleaires, B.P. No. 85, Centre du Tri, 38041 Cedex, Grenoble, France
48. Library, Culham Laboratory, UKAEA, Abingdon, Oxfordshire, OX14 3DB, England
49. Library, FOM-Instituut voor Plasma-Fysica, Rijnhuizen, Edisonbaan 14, 3439 MN Nieuwegein, The Netherlands
50. Library, Institute of Plasma Physics, Nagoya University, Nagoya 64, Japan
51. Library, International Centre for Theoretical Physics, Trieste, Italy
52. Library, Laboratorio Gas Ionizzati, CP 56, I-00044 Frascati (Roma), Italy
53. Library, Plasma Physics Laboratory, Kyoto University, Gokasho, Uji, Kyoto, Japan
54. Plasma Research Laboratory, Australian National University, P.O. Box 4, Canberra, A.C.T. 2000, Australia
55. Thermonuclear Library, Japan Atomic Energy Research Institute, Tokai-mura, Ibaraki Prefecture, Japan

56–163. Given distribution as shown in TIC-4500, Magnetic Fusion Energy (Distribution Category UC-20)